Monthly Notices of the ROYAL ASTRONOMICAL SOCIETY

MNRAS **532,** 3509–3525 (2024) https://doi.org/10.1093/mnras/stae1658
Advance Access publication 2024 July 9

Eccentricity and inclination of massive planets inside low-density cavities: results of 3D simulations

M. M. Romanova,[1,2]★ A. V. Koldoba,[3] G. V. Ustyugova,[4] C. Espaillat[5] and R. V. E. Lovelace[1,2]

[1]*Department of Astronomy, Cornell University, Ithaca, NY 14853-6801, USA*
[2]*Carl Sagan Institute, Cornell University, Ithaca, NY 14853-6801, USA*
[3]*Moscow Institute of Physics and Technology, Dolgoprudny, Moscow Region 141700, Russia*
[4]*Keldysh Institute for Applied Mathematics, Moscow 125047, Russia*
[5]*Department of Astronomy, Boston University, 725 Commonwealth Avenue Boston, MA 02215, USA*

Accepted 2024 July 3. Received 2024 July 2; in original form 2024 February 14

ABSTRACT

We study the evolution of eccentricity and inclination of massive planets in low-density cavities of protoplanetary discs using three-dimensional (3D) simulations. When the planet's orbit is *aligned* with the equatorial plane of the disc, the eccentricity increases to high values of 0.7–0.9 due to the resonant interaction with the inner parts of the disc. For planets on *inclined* orbits, the eccentricity increases due to the Kozai–Lidov mechanism, where the disc acts as an external massive body, which perturbs the planet's orbit. At small inclination angles, $\lesssim 30^\circ$, the resonant interaction with the inner disc strongly contributes to the eccentricity growth, while at larger angles, eccentricity growth is mainly due to the Kozai–Lidov mechanism. We conclude that planets inside low-density cavities tend to acquire high eccentricity if favourable conditions give sufficient time for growth. The final value of the planet's eccentricity after the disc dispersal depends on the planet's mass and the properties of the cavity and protoplanetary disc.

Key words: accretion discs – hydrodynamics – planet-disc interactions – protoplanetary discs.

1 INTRODUCTION

Many exoplanets have high eccentricities of their orbits. Giant planets have eccentricities covering the whole range from zero to near unity (e.g. Marcy et al. 2005; Kane et al. 2012; Sagear & Ballard 2023). The phenomenon of non-zero eccentricities has yet to be understood.

Eccentricity and inclination may grow due to the gravitational interaction between planets (e.g. Rasio & Ford 1996; Lin & Ida 1997; Papaloizou & Terquem 2001; Chatterjee et al. 2008; Jurić & Tremaine 2008; Mustill, Davies & Johansen 2017; Anderson, Lai & Pu 2020; Li et al. 2021) or due to secular perturbations from exterior stellar or planetary companions due to Kozai–Lidov mechanism (Kozai 1962; Lidov 1962; Holman, Touma & Tremaine 1997; Takeda & Rasio 2005; Fabrycky & Tremaine 2007; Anderson, Storch & Lai 2016; Anderson & Lai 2017). On the other hand, they may vary due to the interaction of a planet with an accretion disc (e.g. Goldreich & Tremaine 1980).

A planet in the low-density cavity interacts with the inner disc by eccentric Lindblad resonances (ELRs), and the eccentricity increases (e.g. Goldreich & Tremaine 1980; Artymowicz et al. 1991; Goldreich & Sari 2003; Ogilvie & Lubow 2003; Teyssandier & Ogilvie 2016). A low-density cavity may be supported by various physical mechanisms, e.g. by the magnetosphere of the star (e.g. Königl 1991; Hartmann 2000; Romanova & Lovelace 2006; Romanova & Owocki 2015), magnetic wind from the star (e.g. Lovelace, Romanova & Barnard 2008; Schnepf et al. 2015; Bai 2016; Wang & Goodman 2017; Elbakyan et al. 2022), or evaporation of the inner disc due to UV radiation (e.g. Dullemond et al. 2007).

A number of two-dimensional (2D) numerical simulations have been performed that show that eccentricity can increase due to the disc–planet resonant interaction (e.g. Papaloizou, Nelson & Masset 2001; DÁngelo, Lubow & Bate 2006; Kley & Dirksen 2006; Rice, Armitage & Hogg 2008; Bitsch et al. 2013a; Dunhill, Alexander & Armitage 2013; Ragusa et al. 2018; Debras, Baruteau & Donati 2021; Baruteau et al. 2021). In many simulations, only a small value of eccentricity has been obtained, $e \sim 0.1$–0.25 (e.g. Papaloizou et al. 2001; DÁngelo et al. 2006; Kley & Dirksen 2006). Larger eccentricity $e \approx 0.4$ has been observed by Debras et al. (2021) who were able to keep the disc-cavity boundary at the same location by setting a high/low viscosity in the cavity/disc, and by Rice et al. (2008) who fixed the disc-cavity boundary and calculated the gas evolution only in the disc. The eccentricity of the planet may also increase or decrease due to the exchange of eccentricity between the planet and the disc (e.g. Teyssandier & Ogilvie 2016; Ragusa et al. 2018; Li & Lai 2023).

In our earlier work, we used 2D simulations to investigate the eccentricity growth of massive planets located in the cavity with the fixed disc-cavity boundary (Romanova et al. 2023, hereafter R23). We examined a wide range of parameters and observed that the eccentricity typically increases to high values of $\sim$0.6–0.8. We investigated different resonances responsible for eccentricity growth and derived the dependence of the eccentricity growth on various parameters. Simulations confirmed the

★ E-mail: romanova@astro.cornell.edu

theoretically-predicted result that the eccentricity growth rate is proportional to the density (characteristic mass) of the disc. Therefore, simulations are scalable and can be performed for denser discs during a shorter simulation time. These findings opened a path for more realistic 3D simulations of the disc–planet interaction.

This paper shows the results of our global 3D simulations of the disc–planet interaction. We did not fix the disc-cavity boundary and calculate the gas flow inside and outside the cavity. The low-density cavity has been supported by the equilibrium initial conditions and a low disc viscosity. Simulations confirmed that the eccentricity may increase to very high values of $e \sim 0.7$–0.9. We investigate the dependence of the growth rate of eccentricity on different factors, such as the planet's mass and the density, viscosity, and mass of the planet. In models with more massive planets and denser discs, the torques are higher, and eccentricity increases more rapidly. In models with lower grid resolution and higher viscosity, the resonances are not well resolved, and the eccentricity growth is slower.

We also investigate the evolution of the eccentricity and inclination of planets in *inclined* orbits. Terquem & Ajmia (2010) have shown that the orbit of an inner planet can be perturbed by a remote massive disc due to the Kozai–Lidov mechanism, similar to that when the perturber is a distant massive planet or a star. They supported their theoretical findings with *N*-body numerical simulations (see also Teyssandier, Terquem & Papaloizou 2013). In their simulations, the external disc has been fixed. In our work, we calculate the general 3D hydrodynamic model where the density distribution in the disc changes due to the disc–planet interaction. We observed that the eccentricity increases and oscillates due to the Kozai–Lidov effect. We investigated the dependence of the eccentricity growth on the inclination of the orbit and other parameters.

The plan of the paper is as follows: In Section 2, we describe the problem set-up and our numerical model. In Sections 3 and 4, we show the results of simulations in cases of aligned and inclined orbits of the planet. We conclude in Section 6.

2 PROBLEM SETUP AND NUMERICAL MODEL

We place a star of mass M_* in the centre of the coordinate system. We use a 3D grid in cylindrical coordinates (r, ϕ, z). We place a low-density cavity at radii $R_{\rm in} < r < r_{\rm cav}$, and high-density disc at radii $r_{\rm cav} < r < R_{\rm o}$, where $R_{\rm in}$ and $R_{\rm o}$ are the inner and outer boundaries of the simulation region.

We solve a problem in dimensionless form. We measure distances in units of $r_0 = r_{\rm cav}$. The inner and outer boundaries are $R_{\rm in} = 0.3$ and $R_{\rm o} = 18$. The reference mass is the mass of the star, $M_0 = M_* = {\rm M}_\odot$, where we take a Solar mass star as a base. The reference velocity is given by $v_0 = \sqrt{GM_0/r_0}$. The time is measured in Keplerian periods of rotation at $r = r_0$: $P_0 = 2\pi r_0/v_0$. The reference density is $\rho_0 = M_0/r_0^3$ and the reference surface density is $\Sigma_0 = M_0/r_0^2$. The reference pressure is $p_0 = \rho_0 v_0^2$. We also determine the dimensionless mass of the inner disc, $q_{\rm d}$, such that the dimensional characteristic mass of the inner disc is $M_{\rm d0} = q_{\rm d} M_0$, where $M_{\rm d0} = \Sigma_{\rm d0} r_0^2$ is characteristic mass of the inner disc[1] and, where $\Sigma_{\rm d0} = q_{\rm d}\Sigma_0$ is the characteristic surface density, and therefore $q_{\rm d} \equiv \widetilde{\Sigma}_{\rm d} = \Sigma_{\rm d0}/\Sigma_0$ is also a dimensionless surface density of the disc at the reference point $r = r_0$. We drop tilde and hereafter use the dimensionless surface density $\Sigma_{\rm d}$ as a parameter that characterizes typical mass of the inner disc. In current simulations, we take $\Sigma_{\rm d} = 3 \times 10^{-2}$. For practical applications, we use the more realistic value of $\Sigma_{\rm d} = 10^{-4}$ (see Table 1).

We place a planet of mass $m_{\rm p} = q_{\rm p} M_0 = 5 \times 10^{-3} M_0 = 5 M_{\rm Jup}$ inside the cavity at the orbit with the semimajor axis $a_0 = 0.6$. We take masses $m_{\rm p} = 3 M_{\rm Jup}$ and $10 M_{\rm Jup}$ in test simulation runs. We take an orbit with a small initial eccentricity $e = 0.02$. It helps to decrease the eccentricity damping by the 1st order corotation torque (e.g. Goldreich & Sari 2003; Ogilvie & Lubow 2003). A planet is placed either in the equatorial plane of the disc at zero inclination angle, $i_0 = 0^\circ$, or in inclined orbit with inclination angles from $i_0 = 5^\circ$ up to 75°.

2.1 Initial disc-cavity equilibrium

We calculate the equilibrium distribution of density and pressure in the disc and cavity using an approach described in Romanova et al. (2019). In this approach, it is suggested that the disc has a high density, $\rho_{\rm d}$ while the cavity has very low density, $\rho_{\rm cav} \ll \rho_{\rm d}$. To support this configuration, we take a high temperature in the cavity and a low temperature in the disc, such that at the disc-cavity boundary, the gas pressure in the disc equals the gas pressure in the cavity, $p_{\rm d} = p_{\rm cav}$.

To construct our initial condition, we first determine the equilibrium in the equatorial plane. The initial density distribution is given by

$$\rho(r, 0) = \begin{cases} \rho_{\rm cav} & \text{if } r < r_{\rm cav} \\ \rho_{\rm d} \left(\frac{r}{r_{\rm cav}}\right)^{-n} & \text{if } r \geq \boldsymbol{r}_{\rm cav}. \end{cases} \quad (1)$$

Here, $\rho_{\rm cav}$ is the density in the cavity and $\rho_{\rm d}$ is the disc density near the cavity boundary, $r = r_{\rm cav}$. Parameter n specifies the radial profile of the disc density. We take a similar distribution for pressure in the disc and cavity.

We take a disc with semithickness $h/R = 0.03$ (determined at $r = r_{\rm d}$) and derive the temperature in the disc from the condition: $(h/R)_{\rm d} = (c_{\rm s}/v_{\rm K})_{\rm d}$, where $c_{\rm s}$ and $v_{\rm K}$ are the sound speed and Keplerian velocities at $r = r_{\rm d}$. Using our dimensionalization ($GM = 1$, $r_0 = r_{\rm cav}$, $v_{\rm K0} = v_0 = 1$), we obtain the temperature at the inner edge of the disc: $T_{\rm d} = c_{\rm s}^2 = (h/R)^2 = 0.0009$. We determine the dimensionless density $\rho_{\rm d}$ at $r = r_{\rm d}$ ($\rho_{\rm d} = 0.4$ in most of our simulations). We take much lower density in the cavity, $\rho_{\rm cav} = 10^{-3}\rho_{\rm d}$.

At the inner edge of the disc ($r = r_{\rm d}$), we take an equal pressure for the disc and cavity in the equatorial plane: $p_{\rm d} = p_{\rm cav}$. This condition provides a zero pressure gradient force at the boundary and the initial equilibrium between the disc and cavity.

The dimentionless temperature is related to density and pressure by the ideal gas law, $\mathcal{R}T(r) = p(r)/\rho(r)$. Therefore, $T_{\rm d}\rho_{\rm d} = T_{\rm cav}\rho_{\rm cav}$ and the temperature in the cavity $T_{\rm cav} = 10^3 T_{\rm d}$ is much higher than that in the disc.[2]

Initially, the disc is isothermal. The temperature in the cavity is also constant. Subsequently, at $t > 0$, we calculate the temperature distribution using the energy equation.

In our model, the cavity has a very low density, 10^3 times lower than in the disc. A planet in the low-density cavity excites the zero-

[1]Note that many authors use the total mass of the disc in their definition of $q_{\rm d}$ (e.g. Teyssandier & Ogilvie 2016; Ragusa et al. 2018).

[2]In protoplanetary discs, the temperature may be low in both the disc and cavity (excluding cases where cavities are carved by stellar wind or high-energy radiation from the star). We note that the condition of equal pressure (a high temperature in the cavity) is not a necessary condition for the final equilibrium because the main forces that support the disc are gravitational and centrifugal forces, while the pressure gradient force is much smaller.

Table 1. *Top rows:* reference values calculated for different sizes of the disc-cavity boundary $r_{\rm cav}$. *Middle rows:* initial values of density and surface density taken in the model. *Bottom rows:* Projected values, where we took a small value of the surface density, $\Sigma_{\rm d} = 10^{-4}$.

Reference unit		Reference values		
Reference distance $r_0 = r_{\rm cav}$	r_0 [au]	0.1	1.0	10
Reference velocity	v_0 [km s^{-1}]	94.3	29.8	9.4
Reference period	P_0 [d]	11.56	365.3	11599 (31.78 yrs)
Reference density	ρ_0 [g cm^{-3}]	5.9×10^{-4}	5.9×10^{-7}	5.9×10^{-10}
Reference surface density	Σ_0 [g cm^{-2}]	8.9×10^{8}	8.9×10^{6}	8.9×10^{4}
		Values in reference models at $\Sigma_{\rm d} = 3.0 \times 10^{-2}$		
Initial density at $r = r_{\rm cav}$	$\rho_{\rm d0}$ [g cm^{-3}]	2.4×10^{-4}	2.4×10^{-7}	2.3×10^{-10}
Initial surface density	$\Sigma_{\rm d0}$ [g cm^{-2}]	2.7×10^{7}	2.7×10^{5}	2.7×10^{3}
		Projected values at $\Sigma_{\rm d} = 1.0 \times 10^{-4}$		
Initial density at $r = r_{\rm cav}$	$\rho_{\rm dp}$ [g cm^{-3}]	8.0×10^{-7}	8.0×10^{-10}	8.0×10^{-13}
Initial surface density	$\Sigma_{\rm dp}$ [g cm^{-2}]	8.9×10^{4}	8.9×10^{2}	8.9

order Lindblad resonances responsible for the migration. However, the torques are proportional to the density (e.g. Goldreich & Tremaine 1979) and are 10^3 times smaller than torques acting on a planet migrating inside the disc. In simulations, we observed that a planet migrates inward as long as some of the Lindblad resonances are located inside the disc. However, migration stops when all resonances are located inside the cavity, and ELRs start acting. The high temperature in the cavity does not influence the planet's migration in the cavity.[3]

Next, we assume that there is a hydrostatic equilibrium in the vertical direction and build the 3D distribution of density:

$$\rho(r, z) = \rho(r, 0) \exp\left(\frac{\Phi(r, 0) - \Phi(r, z)}{\mathcal{R}T(r, 0)}\right), \tag{2}$$

where $\Phi(r, z) = -GM_*/(r^2 + z^2)^{1/2}$ is the gravitational potential of the star. The expression for pressure is analogous. The azimuthal velocity v_ϕ is determined from the balance between gravity and pressure gradient forces in the radial direction:

$$v_\phi(r, z) = \sqrt{r\left(\frac{\partial \Phi}{\partial r} + \frac{1}{\rho}\frac{\partial p}{\partial r}\right)}. \tag{3}$$

These formulae allow us to start from a quasi-equilibrium configuration for the disc and the cavity.

We obtain the surface density distribution in the disc by integrating the volume density ρ in the z-direction:

$$\Sigma = \int \rho \, {\rm d}z \propto H\rho \propto \frac{c_{\rm s}\rho}{\Omega} \propto \frac{\sqrt{p\rho}}{\Omega} \propto r^{-s}, \tag{4}$$

where, $c_{\rm s} \propto \sqrt{p/\rho}$ is the sound speed and $s = \frac{3-2n}{2}$.

2.2 Calculation of the planet's orbit

We calculate the orbit of the planet, taking into account the interaction of a planet with the star and the disc. We use the earlier developed approaches (e.g. Kley 1998; Masset 2000; Kley & Nelson 2012; Comins et al. 2016; Romanova et al. 2019). We find the position $\boldsymbol{r}_{\rm p}$ (the radius vector from the star to the planet) and velocity $\boldsymbol{v}_{\rm p}$ of the planet at each time-step solving the equation of motion:

$$M_{\rm p}\frac{{\rm d}\boldsymbol{v}_{\rm p}}{{\rm d}t} = -\frac{GM_*M_{\rm p}}{|\boldsymbol{r}_{\rm p}|^3}\boldsymbol{r}_{\rm p} - \frac{GM_{\rm p}^2}{|\boldsymbol{r}_{\rm p}|^3}\boldsymbol{r}_{\rm p} + \boldsymbol{F}_{\rm disc\to p}. \tag{5}$$

The first term on the right-hand side represents the gravitational force from the star. The middle term accounts for the fact that the coordinate system is centred on the star and is not inertial.

$$\boldsymbol{F}_{\rm disc\to p} = \int \frac{GM_{\rm p}}{|\boldsymbol{r} - \boldsymbol{r}_{\rm p}|^3}(\boldsymbol{r} - \boldsymbol{r}_{\rm p})\rho r \, {\rm d}r \, {\rm d}\phi \, {\rm d}z \tag{6}$$

is a cumulative force acting from the disc to the planet.

We calculate the planet's orbital energy and angular momentum per unit mass using the calculated values of $\boldsymbol{r}_{\rm p}$ and $\boldsymbol{v}_{\rm p}$:

$$E_{\rm p} = \frac{1}{2}|\boldsymbol{v}_{\rm p}|^2 - \frac{GM_*}{r_{\rm p}} \text{ and } \boldsymbol{L}_{\rm p} = \boldsymbol{r}_{\rm p} \times \boldsymbol{v}_{\rm p}. \tag{7}$$

We use these relationships to calculate the semimajor axis and eccentricity of the planet's orbit at each time-step:

$$a_{\rm p} = -\frac{1}{2}\frac{GM_*}{E_{\rm p}} \text{ and } e_{\rm p} = \sqrt{1 - \frac{L_{\rm p}^2}{GM_*a_{\rm p}}}. \tag{8}$$

We calculate the inclination angle of the orbit as

$$i_{\rm p} = \arccos\left(\frac{L_{\rm zp}}{L_{\rm p}}\right), \tag{9}$$

where $L_{\rm zp}$ is the z-component of the angular momentum.

2.3 Evolution of the disc

The evolution of the disc has been calculated using earlier-developed approaches (Koldoba et al. 2016; Romanova et al. 2019). Below, we briefly describe the numerical model. We model the evolution of the accretion disc using 3D equations of hydrodynamics:

$$\frac{\partial \vec{U}}{\partial t} + \nabla \cdot \vec{F}(\vec{U}) = \vec{Q}, \tag{10}$$

where $\vec{U}$ is the vector of conserved variables and $\vec{F}(\vec{U})$ is the vector of fluxes:

$$\vec{U} = [\rho, \rho S, \rho\vec{v}]^T, \quad \vec{F}(\vec{U}) = [\rho\vec{v}, \rho\vec{v}S, \mathsf{M}]^T, \tag{11}$$

and $\vec{Q} = [0, 0, -\rho\nabla\Phi]$ is the vector of source terms; ρ is the density, $\vec{v}$ is the velocity vector, $S \equiv p/\rho^\gamma$ is the entropy function; we take $\gamma = 5/3$ in all models, Φ is the gravitational potential of the star–planet system and $\boldsymbol{M}$ is the momentum flux tensor, with components $M_{ij} = \rho v_i v_j + \delta_{ij}p - \tau_{ij}$, where p is the fluid pressure and δ_{ij} is

[3]Thermodynamics, viscosity, and irradiation of the disc by a star may change the direction of migration of a planet located in the disc (e.g. Bitsch et al. 2013b; Pierens & Raymond 2016). However, in the low-density cavity, the influence of the high-temperature gas on the planet's migration is negligibly small.

Table 2. Parameters in main reference models. We name reference models using parameters n and i_0: $n1.5i0$, $n1.8i0$, $n1.5i45$, $n1.8i45$, etc.

Parameter	Value
mass of the planet (in $M_\odot$)	$q_p = 5 \times 10^{-3}$
mass of the planet in Jupiter mass	$M_p = 5$
semithickness of the disc	$h = 0.03$
reference surface density	$\Sigma_d = 3 \times 10^{-2}$
coefficient of viscosity	$\alpha = 3 \times 10^{-4}$
slope in ρ distribution	$n = 1.5$ or 1.8
semimajor axis of the planet	$a_0 = 0.6$
initial eccentricity	$e_0 = 0.02$
inclination of planet's orbit	$i_0 = 0^\circ$ or 45°

the Kronecker symbol; τ_{ij} is the tensor of viscous stresses (we take into account only $r\phi$ and $z\phi$ components). In our code, we use the entropy balance equation instead of the full energy equation. We include a viscosity term, with the viscosity coefficient in the form of α-viscosity, $\nu_{vis} = \alpha c_s H$ (Shakura & Sunyaev 1973).

The equations of hydrodynamics are integrated numerically using an explicit conservative Godunov-type numerical scheme (Koldoba et al. 2016). At the external boundaries, we use 'free' boundary conditions $\partial A/\partial r = 0$ and $\partial A/\partial z = 0$ for all variables A. At these conditions, matter freely flows out of the simulation region. We place an additional condition: we forbid the inward flow of matter into the simulation region. At the inner boundary, we use fixed boundary conditions. They provide better results compared with the free conditions. The density in the cavity is very low, and only an insignificant amount of matter accumulates at the boundary during the simulation run. We also use the procedure of damping waves at the inner and outer boundaries, following Fromang, Terquem & Nelson (2005). In addition, we place an exponential cut to the density distribution at the radius $r = 0.7R_o$ (with the width of exponential decay of $0.2R_o$) to be sure that the external boundary does not influence the result.

The simulation region represents a flat cylinder that stretches in the radial direction between the inner and outer boundaries, $0.3 < R < 18$, and in the vertical direction between values of $-1.5 < z < 1.5$. The grid is evenly spaced in the azimuthal and vertical directions, where the number of grid cells in most of the simulations is $N_\phi = 300$ and $N_z = 72$, respectively. In the radial direction, $N_r = 168$, and the size of grids increases with the distance from the star such that the grids have approximately a square shape. The code is parallelized using MPI. Typical number of processors per one simulation run is 280.

2.4 Reference models

In the reference models, we take a planet of mass $M_p = 5M_J$ ($q_p = 5 \times 10^{-3}$) and a disc with a reference surface density $\Sigma_d = 3 \times 10^{-2}$, viscosity coefficient $\alpha = 3 \times 10^{-4}$ and semithickness of the disc $h = H/r = 0.03$ (determined at the inner edge of the disc, $r = r_{cav}$). We take two values of slopes in the equatorial density distribution $n = 1.5$ and 1.8, which correspond to slopes in the surface density distribution: $s = 0$ and 0.3, respectively. We place a planet in the orbit with a semimajor axis $a_0 = 0.6$ (see Table 2 for parameters in Reference model). In test models of R23, we observed that in models with $0.6 < a_0 < 1.0$, the result is very similar. However, initially, a planet migrates inward due to the principal 1:2 outer Lindblad resonance (OLR), and only later, when $a_0 \approx 0.6$, the eccentricity starts to increase due to 1:3 ELR. That is why, to save computing time, we place a planet at $a_0 = 0.6$.

We take non-zero initial eccentricity, $e_0 = 0.02$. In test models of R23 with zero eccentricity, there is an interval of time where the eccentricity increases, but slowly, due to the opposing action of the 1:2 eccentric corotation resonance (ECR), which damps the eccentricity. However, the ECR resonance is saturated in models with a small initial eccentricity (e.g. Goldreich & Sari 2003; Ogilvie & Lubow 2003). To save computing time, we take $e_0 = 0.02$ in all our models.

We take the inclination angle of the orbit $i_0 = 0$ in models where a planet is located in the plane of the disc and different values of i_0 in models where we investigate inclined orbits. We name reference models using parameters n and i_0 ($n1.5i0$, $n1.8i0$, $n1.5i45$, etc.) In these models, we take common parameters shown in Table 2. If we change other parameters, then we specify them in the text and supplementary tables.

2.5 Testing initial equilibrium

First, we take a planet with zero mass $m_p = 0$ and test the stability of our initial conditions determined by equations (1)–(4). Fig. 1 compares density distributions at different moments in time. Right-hand panels show rz projections of the density distribution at $t = 0$ (top panel) and at moments $t = 100$ and 400. The left-hand panels show the radial distribution of the equatorial density ρ (top) and surface density Σ. One can see that initially, the density distribution changed slightly, but at later times, it stayed approximately the same. Therefore, the initial conditions described in Section 2.1 provide a good equilibrium between matter in the disc and cavity. The simulation time of $t = 400$ is longer than the duration of our simulation runs. We conclude that this initial set-up can be used as a base for our 3D simulations. These initial conditions may directly describe inner cavities around the star formed by the magnetosphere, stellar wind, or high-energy radiation from the star. Cavities at larger distances from the star may have dust, pebbles, and regions of forming planets. In cavities, located away from the star, the temperature can be low. In our model, the density in the cavity is so low that neither density nor high temperature influence the dynamics of the planet. Planet interacts gravitationally only with a star and the disc.

3 PLANETS AT ALIGNED ORBITS

First, we take a reference model $n1.5i0$ with typical reference parameters (see Table 2) and place an orbit of the planet in the equatorial plane of the disc (at inclination angle $i_0 = 0$). We keep a planet in a fixed orbit during the first 10 rotations of the inner disc and then release it. The 1st row from the top of Fig. 2 shows the surface density distribution, Σ, in the inner part of the simulation region, near the cavity. One can see two tight spiral waves at $t = 50$ and three waves at $t = 70$, 90, 120. These waves are similar to waves observed in 2D simulations of R23. They correspond to $m = 2$ and 3 modes of the ELR. They drive the eccentricity of the planet up to $e \approx 0.8$.

The 2nd row from the top shows the surface density distribution in the whole simulation region. One can see that a one-armed density wave forms in the inner disc and propagates to large distances.

The 3rd row shows that the $m = 2$ and 3 resonant ELR density waves also present in the equatorial density distribution. The 4th row shows the equatorial density distribution in the whole region.

The bottom left-hand panels of the same figure show the temporal evolution of orbital parameters (top) and coordinates of the planet (bottom). One can see that the eccentricity increases during $t \approx 120$,

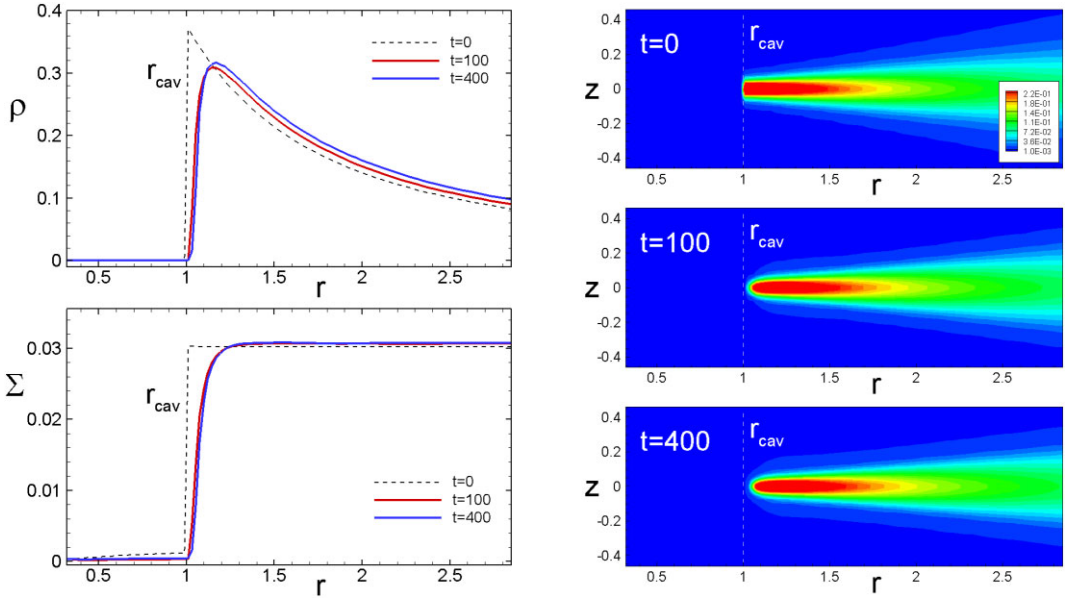

Figure 1. *Left-hand panel:* Linear distribution of the density ρ and surface density Σ in the inner disc in models with zero planet mass $m_{\rm p} = 0$ at $t = 0$ (dashed line) and 100, 400. *Right-hand panel:*rz-slices of the density distribution ρ, at the same moments in time.

reaches $e \approx 0.8$, and then varies in the interval of $0.7 \lesssim e \lesssim 0.9$. The semimajor axis initially decreases and then increases.

We use the Cartesian coordinates to track the position of the planet, where coordinates x and y are located in the equatorial plane of the disc, and the z-coordinate coincides with the z-coordinate of the cylindrical system. One can see that x and y coordinates increase, and at $t \approx 120$, they reach the inner parts of the disc-cavity boundary at $r \approx 1$–1.1. Oscillations of x and y coordinates reflect precession of the planet's orbit with a typical time-scale of $t_{\rm prec} \approx 25$–30 (see more details in Section 5).

The bottom right-hand panels show the rz-slices of the density distribution at $t = 0$ and 120. One can see that during the simulation, the disc changed its structure due to interaction with the planet. Changes are more significant than in the zero-mass planet's model (see Fig. 1). However, the low-density cavity is present, and the disc can be used to investigate the current problem.

When the planet reaches the inner parts of the disc, the eccentricity starts decreasing due to the coorbital corotation torque. At the cavity boundary, this torque is asymmetric and tends to move a planet to larger radii (e.g. Masset et al. 2006; Romanova et al. 2019). This may explain why the semimajor axis increases after $t \approx 120$. The ELR resonances tend to move to larger radii. However, a planet also moves to larger radii. This provides quasi-stationary situation when the eccentricity is high for a while. On the other hand, ELR resonances in the disc become non-axisymmetric, and precession of matter in the inner disc may gradually smear resonances. This also stops the planet's eccentricity growth.[4] The final eccentricity of the planet depends on the particular situation, such as the rate of the disc dispersal.

Fig. 3 shows the same values but in reference model $n1.8i0$, where the surface density decreases with the distance as $\Sigma \sim r^{-0.3}$. One can see that similar ELR resonances are observed in the inner disc. However, the one-armed density wave is weaker.

[4]A planet continues interacting with the disc gravitationally and may exchange its eccentricity with the disc. Ragusa et al. (2018) performed long-lasting 2D simulations of the disc–planet interaction at late states of evolution and low masses of the disc, and observed that a planet and a disc exchange eccentricity quasiperiodically (and in antiphase) for a long time.

3.1 Dependence on parameters

We take reference models $n1.5i0$ and $n1.8i0$ and investigate the eccentricity growth at different parameters (see Table 3 for set of parameters).

3.1.1 Dependence on the mass of the planet

We performed simulations at the lower, $m_{\rm p} = 3M_{\rm J}$ and higher, $m_{\rm p} = 10M_{\rm J}$ mass of the planet. Left-hand panel of Fig. 4 shows that in both models, the eccentricity increased up to $e \approx 0.8$–0.9. However, the eccentricity growth rate is smaller/larger in models with a smaller/larger planet mass. The right-hand panels of the same figure show that the amplitude of ELR density waves is larger in models with larger planet mass. These simulations show that the torque increases with the planet's mass, as predicted in theory.

3.1.2 Dependence on viscosity

We performed test simulations at several values of the α-parameter of viscosity from $\alpha = 10^{-2}$ up to 3×10^{-4}. The left-hand panel of Fig. 5 shows the eccentricity variation at different α. The results are almost the same at $\alpha = 10^{-3}$ and 3×10^{-4}. However, the eccentricity increases slower when $\alpha = 3 \times 10^{-3}$ and even slower when $\alpha = 10^{-2}$. Right-hand panels show that the ELR density waves becomes more smeared in models with higher values of α taken at moments $t = 50$ (top panels) and 80 (bottom panels). This result is similar to our 2D simulations (R23). Both types of simulations show that the action of ELRs decreases at higher viscosities in the disc.

3.1.3 Dependence on the grid resolution

The grid resolution taken in our models is $N_{\rm r} \times N_\phi \times N_z = 168 \times 300 \times 72$. For comparison, we calculated models with a lower and

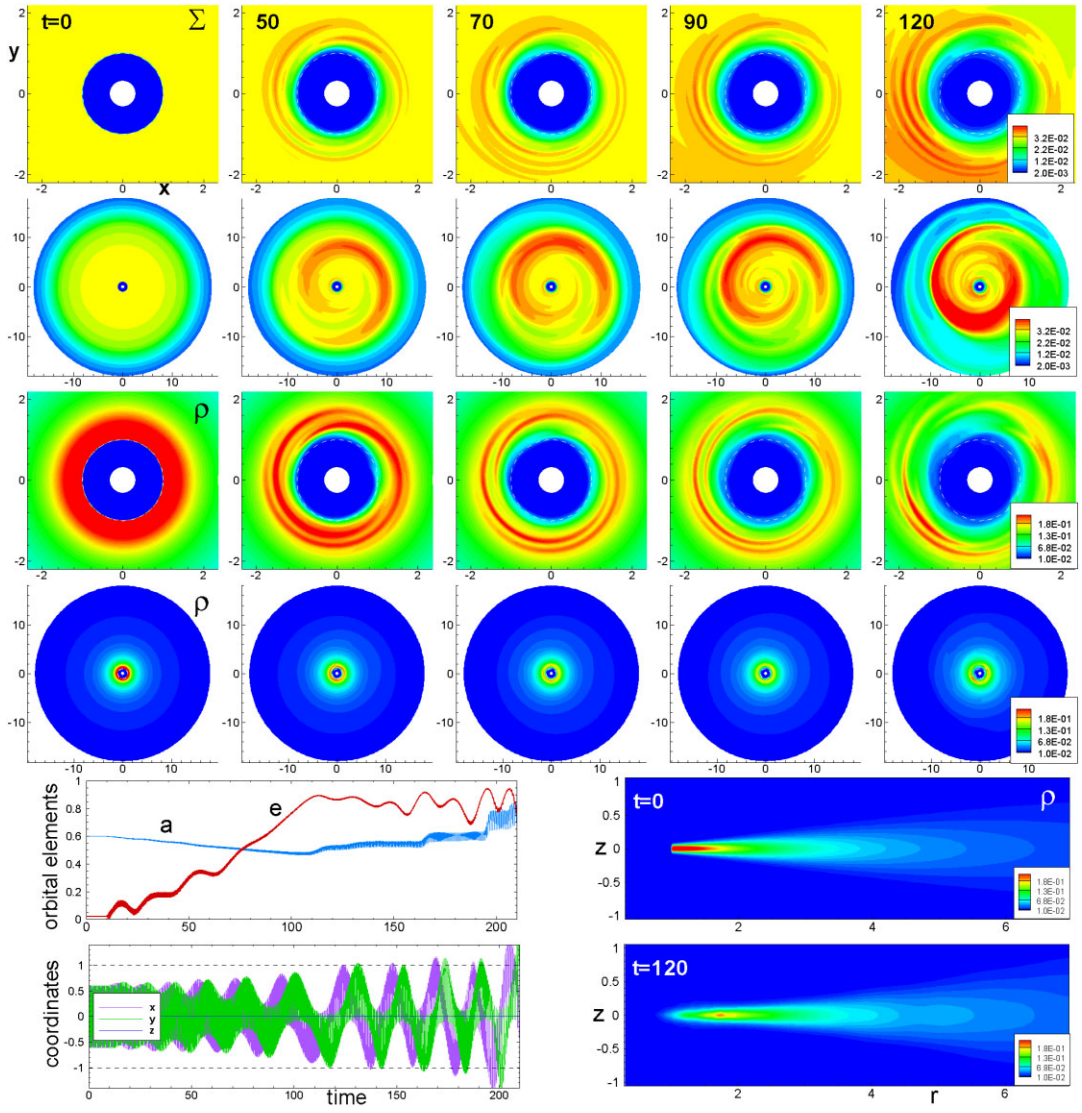

Figure 2. Simulation results of the disc–planet interaction in model $n1.5i0$. The top row of panels shows the surface density distribution Σ in the inner part of the simulation region at different moments in time, t. The 2nd row shows the same but in the whole simulation region. The 3rd and 4th rows show the same but for the volume density distribution ρ in the equatorial plane. The blue and red colours show the lowest/highest values of surface density and density. *Bottom left-hand panels*: Top: temporal evolution of the semimajor axis, a, and eccentricity, e. Bottom: temporal evolution of the planet's coordinates, x, y, z. The time is measured in periods of Keplerian rotation at the initial location of the cavity boundary, $r_{\rm cav} = 1$. *Bottom right-hand panels:* density distribution in the rz-plane at $t = 0$ and 120.

Table 3. A set of parameters used to test a reference model $n1.5i0$.

	Testing models with aligned orbits ($i_0 = 0$) at different parameters				
Mass of the planet	$m_{\rm p}(M_{\rm J})$	0	3	5	10
Viscosity	α-parameter	3×10^{-4}	1×10^{-3}	3×10^{-3}	1×10^{-2}
Grid resolution	N_ϕ	100	200	300	400
Slope in the density distribution	n	1.5	1.8	2	2.5

higher grid resolutions: $70 \times 100 \times 24$, $119 \times 200 \times 48$, and $217 \times 400 \times 96$.

Left-hand panel of Fig. 6 shows that at the higher grid resolution ($N_\phi = 400$), the curve for eccentricity evolution almost coincides with that for $N_\phi = 300$ grid. However, the simulations are 2.6 times slower. At the lower grid resolution ($N_\phi = 100$ and 200), the simulations are faster. However, the eccentricity increases increases slower or decreases (see pink and green lines in the figure). That is why we chose the grid $N_\phi = 300$ in our simulations.

Both 2D and 3D simulations show the necessity of high grid resolution while modelling ELRs. Models with a low grid resolution may show a lower eccentricities compared with the higher grid resolution and, hence, may underestimate the final value of the planet eccentricity.

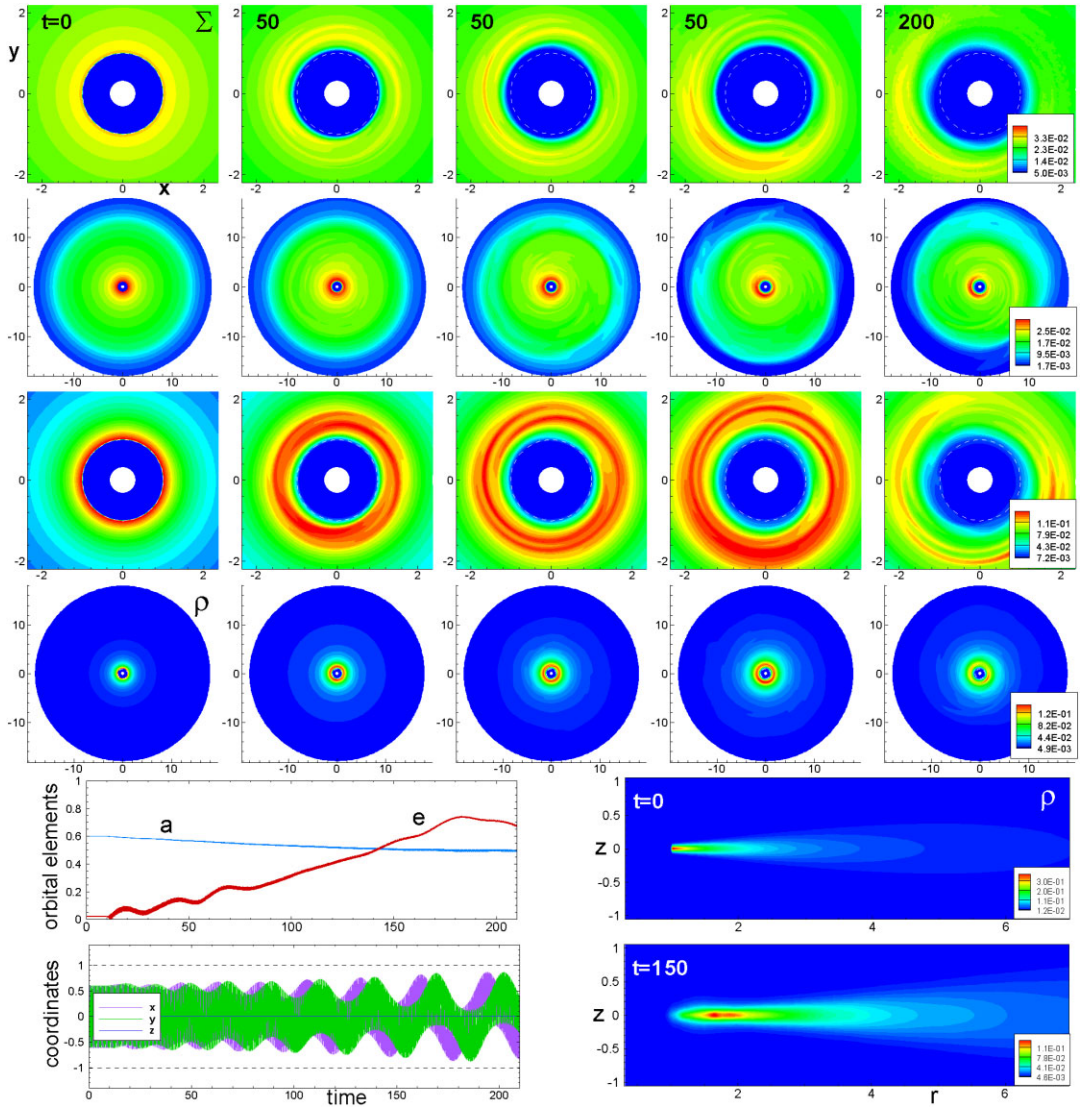

Figure 3. Same as in Fig. 2 but for reference model $n1.8i0$. Note that we use slightly different colour bars at different scales to show the fine structure of ELRs in enlarged plots and features in the whole disc in expanded plots.

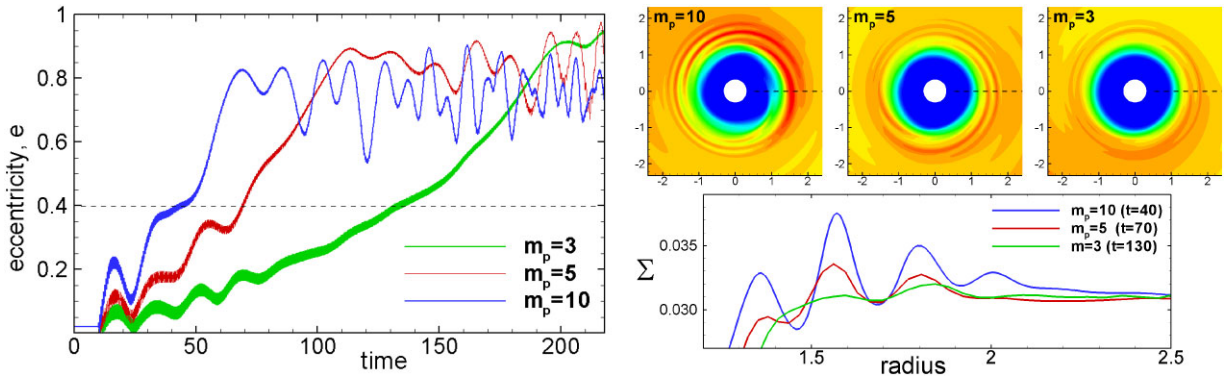

Figure 4. *Left-hand panel:* Eccentricity evolution in the model $n1.5i0$ at different masses of the planet, $m_{\rm p}$. The time is measured in periods of Keplerian rotation at the initial location of the cavity boundary, $r_{\rm cav} = 1$. *Right-hand panels:* Top: the surface density distribution for these models at moments when $e \approx 0.4$. Bottom: The surface density distributions in the equatorial plane of the above figures along x-direction (marked in dashed lines).

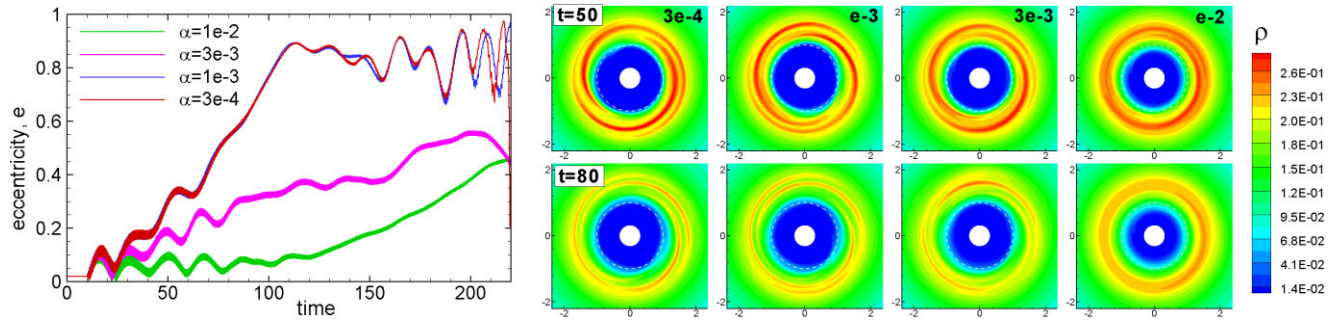

Figure 5. *Left-hand panel:* Eccentricity evolution in model $n1.5i0$ but with different values of the α-parameter of viscosity in the disc. *Right-hand panels:* Equatorial density distribution at different values of α-parameter at times $t = 50$ (top panels) and 80 (bottom panels).

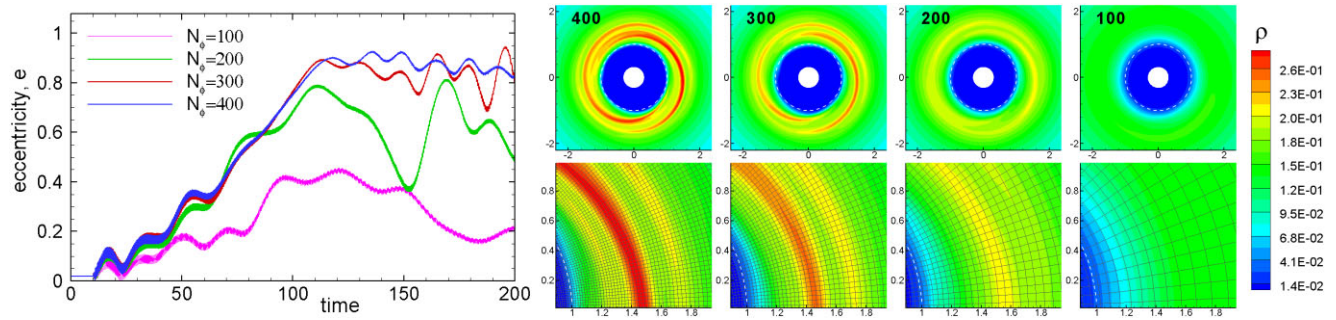

Figure 6. *Left-hand panel:* Eccentricity evolution in models with parameters of the reference model $n1.5i0$ but with different grid resolutions $N_\phi = 400, 300, 200, 100$. *Right-hand panels: Top:* Equatorial density distribution at $t = 50$ and at different grids. *Bottom:* the same, but a part of the region and the grid are shown.

Right-hand panels of Fig. 6 show the equatorial density distribution after $t = 50$ rotations in simulations with different grids. The bottom panels show a part of the simulation region and the grid. One can see that at grid resolutions $N_\phi = 400$ and 300, the ELR density waves are well resolved (with many grids across the wave) and are of high density (amplitude, red colour). At the lower grid, $N_\phi = 200$, the density waves are resolved only by a few grid cells, and the amplitude of waves is smaller (yellow colour). At even a lower grid resolution, $N_\phi = 100$, the grid does not resolve the wave, and we do not observe the wave. We think that at lower grid resolutions, the numerical diffusivity is high and the denser matter of spiral waves diffuses away from their initial positions.

We should note that at the lower density of the inner disc and lower mass of the planet, the torques are weaker, and the grid resolution should be higher to resolve ELRs. For example, in R23, at the low-disc density, $q_{\rm d} = \Sigma_{\rm d} = 3 \times 10^{-4}$, the grid resolution of $N_\phi = 600$ was necessary to resolve ELRs. However, in current 3D simulations where $\Sigma_{\rm d} = 3 \times 10^{-2}$, the disc density is high, and the grid with $N_\phi = 300$ is sufficient.

3.1.4 Dependence on the slope of the density distribution

We compared the eccentricity evolution at different initial slopes of the density distribution in the disc. We took discs with equatorial density distributions $\rho \sim r^{-n}$ with $n = 1.5, 1.8, 2, 2.5$. They correspond to the surface density distributions: $\Sigma \sim r^{-s}$, with $s = 0, 0.3, 0.5, 1$. The right-hand panel of Fig. 7 shows the initial density and surface density distributions with radius. The left-hand panel shows that the eccentricity increases slower in models with steeper slopes in density distribution. We think that the eccentricity growth rate decreases with n because at steeper density distributions, the inner disc mass $\Sigma_{\rm d0} r_0^2$ and the total mass of the disc is smaller. When we increase the density 1.5–2 times, we observe faster eccentricity growth. After multiple experiments with different s, we conclude that the steeper density distribution is not a factor that may stop eccentricity growth.

3.1.5 Comparison of 3D and 2D simulations

We compared the eccentricity evolution in our reference 3D models $n1.5i0$ and $n1.8i0$ with 2D models calculated at the same physical parameters (see Table 2) and the grid. We also compared 3D models with a 2D model of R23 where the cavity radius has been fixed and simulations of the gas flow were performed only at the radius $r > r_{\rm cav}$ (see complete set of parameters in Table 4). The left and right-hand panels of Fig. 8 compare the eccentricity evolution in 3D and 2D simulations in models with $n = 1.5$ and 1.8. One can see that in 2D model 2D-300, the eccentricity increases with the same rate as in the 3D model up to $e \approx 0.2$. Subsequently, it decreases. The eccentricity increases again but does not reach high values, like in the 3D model. In test 2D simulation with a higher grid resolution, $N_\phi = 600$ (model 2D-600), the eccentricity increases faster and reaches higher values than in model 2D-300. In the model with the fixed cavity (2D-cav-600) calculated using R23 approach but at the same parameters as in 3D models, the eccentricity initially increases slower than in 3D, but subsequently, it grows to high values, like in the 3D model (see blue lines in Fig. 8). These simulations stopped when the planet reached the cavity boundary. So, we observed that 2D models with non-fixed boundaries show slower eccentricity growth than 3D models. This phenomenon may be due to the faster eccentricity growth in 3D models, as discussed by Teyssandier & Ogilvie (2016). They found that the eccentricity growth rate due to ELRs is 2–4 orders of magnitude larger in 3D models than in 2D models (see growth rate in adiabatic models in their Table 6). This issue should be studied separately.

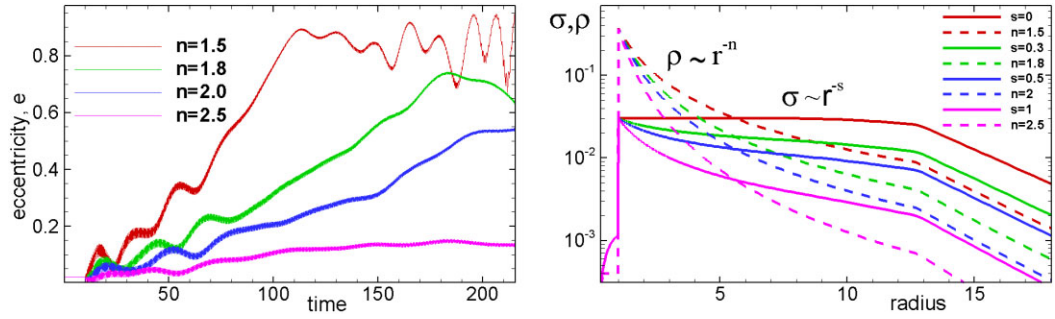

Figure 7. *Left-hand panel:* Eccentricity evolution in models with different slopes n in the equatorial density distributions $\rho \sim r^{-n}$. *Right-hand panel:* Initial equatorial density distribution and surface density distribution, $\Sigma \sim r^{-s}$, with radius in models with different n.

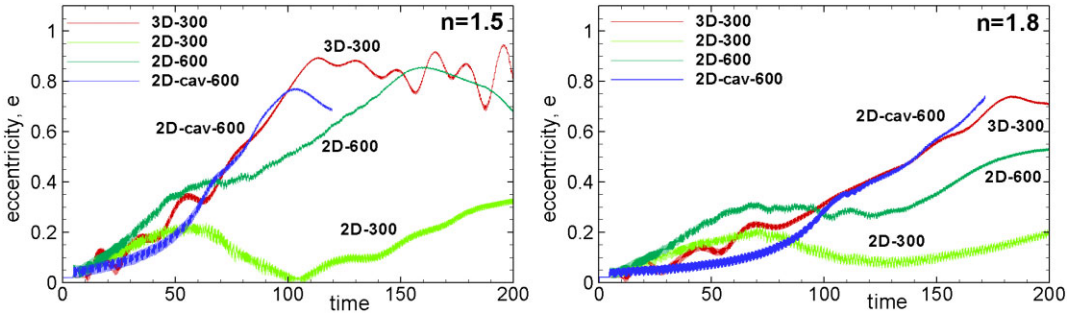

Figure 8. *Left-hand panel:* Eccentricity evolution in 3D model $n1.5i0$ (3D-300) and 2D models with similar parameters. 2D models were calculated at grids $N_\phi = 300$ (2D-300) and 600 (2D-600). A model 2D-cav-600 corresponds to the fixed cavity model of R23 taken at the grid resolution of $N_\phi = 640$ (see also Table 4). *Right-hand panel:* The same but for the model $n1.8i0$.

Table 4. Models used for comparisons of the 3D and 2D models. See comparisons in Fig. 8.

Model grid/dimension	3D-300 3D	2D-600 2D	2D-300 2D	2D-cav-600 2D (fixed cavity)
N_ϕ	300	600	300	640
N_r	168	406	203	336
N_z	72	–	–	–

Table 5. Simulations were performed at a variety of the initial inclination angles of the planet's orbit, i_0, and two values of the density slope in the disc, $n = 1.5$ and 1.8. Names of models are constructed using the values of n and i_0.

Parameter/model	$n1.5i0$	$n1.5i5$	$n1.5i15$	$n1.5i30$	$n1.5i45$	$n1.5i60$	$n1.5i75$
i_0	0°	5°	15°	30°	45°	60°	75°
slope, n	1.5	1.5	1.5	1.5	1.5	1.5	1.5
Parameter/model	$n1.8i0$	$n1.8i5$	$n1.8i15$	$n1.8i30$	$n1.8i45$	$n1.8i60$	$n1.8i75$
i_0	0°	5°	15°	30°	45°	60°	75°
slope, n	1.8	1.8	1.8	1.8	1.8	1.8	1.8

3.1.6 Time-scales of eccentricity growth

From the left-hand panel of Fig. 8, we estimate the eccentricity growth rate in 3D simulations: $t_{\rm ecc}^{-1} = d(\ln e)/{\rm d}t \approx 0.024$ and the time-scale $t_{\rm ecc} \approx 43.48$. This value is relevant to our reference model, where $\Sigma_{\rm d} = 3 \times 10^{-2}$. Our earlier 2D simulations performed in the range of $10^{-2} < \Sigma_{\rm d} < 10^{-4}$ have shown that $t_{\rm ecc}^{-1} \sim \Sigma_{\rm d}$ and also $t_{\rm ecc}^{-1} \sim m_{\rm p}$, which is in accord with theoretical studies (e.g. Goldreich & Tremaine 1980). Here, we project the time-scale of the eccentricity growth to more realistic parameters of $\Sigma_{\rm d} = 10^{-4}$. We also convert time to dimensional units, taking into account that we measure time in units of $P_0 = 2\pi r_0/v_0 = 2\pi r_{\rm cav}^{3/2}/\sqrt{GM_\odot}$. We take $r_{\rm cav} = 10$ au as a reference scale (see Table 1). We obtain the dimensional time of eccentricity growth as:

$$T_{\rm ecc} \approx 4.14 \times 10^5 \,{\rm yr} \left(\frac{r_{\rm cav}}{10\,{\rm au}}\right)^{3/2} \left(\frac{\Sigma_{\rm d}}{10^{-4}}\right)^{-1} \left(\frac{m_{\rm p}}{5M_{\rm J}}\right)^{-1}. \quad (12)$$

Eccentricity will grow if the cavity does not change its position significantly or the disc does not disperse. For example, if the cavity is present during $T_{\rm cav} = 10^6$ yr, then the eccentricity will increase significantly, if $T_{\rm ecc} \lesssim T_{\rm cav}$, or if the cavity radius

$$r_{\rm cav} \lesssim 18\,{\rm au} \left[\left(\frac{T_{\rm cav}}{10^6\,{\rm yr}}\right)\left(\frac{\Sigma_{\rm d}}{10^{-4}}\right)\left(\frac{m_{\rm p}}{5M_{\rm J}}\right)\right]^{2/3}. \quad (13)$$

Planets in a small-sized cavity have a high rate of eccentricity growth. They may have several episodes of eccentricity growth (due to the above-discussed mechanisms) and decay due to local corotation torque when the planet starts entering the inner disc.

4 PLANETS ON INCLINED ORBITS: KOZAI–LIDOV EFFECT

Next, we placed a planet in an inclined orbit with different inclination angles i_0. We observed that the eccentricity typically increases, and it also oscillates. The inclination angle also oscillates, but in antiphase with eccentricity. We suggest that we observe the Kozai–Lidov mechanism, where the disc acts as a massive object that perturbs the planet's orbit.

4.1 Planet–planet/star and planet–disc interaction

Below, we briefly summarize the theory of the Kozai–Lidov mechanism in cases of the planet–planet/star interaction (e.g. Kozai 1962; Lidov 1962; Innanen et al. 1997), and planet–disc interaction (Terquem & Ajmia 2010).

If a planet of mass $m_{\rm p}$ located at an inclined orbit with semimajor axis $a_{\rm p}$, and interacts with a massive object (a planet or a star) of mass $M_{\rm p}$ located at the circular orbit of radius $R_{\rm p} \gg a_{\rm p}$, then the secular perturbation by the distant companion causes the eccentricity $e_{\rm p}$ of the inner planet and the mutual inclination i of two orbits to oscillate in time in antiphase. In this situation, the component of the angular momentum of the inner orbit perpendicular to the orbital plane, L_z is constant and proportional to

$$L_z \propto \sqrt{1-e_{\rm p}^2}\cos i = \text{const}. \tag{14}$$

This equation shows that the decrease of the inclination angle i leads to the increase of the eccentricity $e_{\rm p}$, and vice versa. As a result, the eccentricity and inclination oscillate in the antiphase, and eccentricity can also be pumped to the orbit at the expense of inclination and vice versa.

Terquem & Ajmia (2010) considered the interaction of the planet on the inclined orbit with the external remote disc and noticed that the potential for the planet–planet interaction is similar to that for planet–disc interaction (compare their formulas 4 and 5). They concluded that the Kozai–Lidov mechanism should also operate in the case of the remote discs.

The maximum value of the eccentricity which can be reached during this process is

$$e_{\rm max} = \left(1-\frac{5}{3}\cos^2 i_{\rm c}\right)^{1/2}, \tag{15}$$

and therefore the initial inclination i_0 should be larger than the critical value $i_{\rm c} \approx 39^\circ$ which is determined from condition $\cos^2 i_{\rm c} = 3/5$.

The time $t_{\rm ev}$ to reach $e_{\rm max}$ starting from e_0 in both models is (Innanen et al. 1997):

$$\frac{t_{\rm ev}}{\tau} = 0.42\left(\sin^2 i_0 - \frac{2}{5}\right)^{-1/2} \ln\left(\frac{e_{\rm max}}{e_0}\right), \tag{16}$$

$$\tau = K\left(\frac{R'}{a_{\rm p}}\right)^3\left(\frac{M_*}{M'}\right)\frac{P}{2\pi}, \tag{17}$$

where P is the period of the planet's rotation. For planet–planet/star interaction: $M' = M_{\rm p}$, $R' = R_{\rm p}$, and $K = 1$. For planet–disc interaction (Terquem & Ajmia 2010): $M' = M_{\rm d}$ is the total mass of the disc, $R' = R_o$, and

$$K = \frac{(1+s)(1-\eta^{-s+2})}{(s-2)(1-\eta^{-s-1})}, \tag{18}$$

where $\eta = R_{\rm in}/R_o$, $R_{\rm in}$, and $R_{\rm o}$ are the inner and outer radii of the disc, s, is the power in the surface density distribution (Terquem & Ajmia 2010). If the eccentricity oscillates between e_0 and $e_{\rm max}$ then the period of oscillations is $P_{\rm osc} = 2t_{\rm ev}$.

Terquem & Ajmia (2010) (and also Teyssandier et al. 2013) performed numerical simulations using earlier developed N-body code (Papaloizou & Terquem 2001) and confirmed these theoretical results. In particular, they have shown that $t_{\rm ev}$ increases when $R_{\rm o}$ increases, and also $t_{\rm ev}$ increases when the disc mass $M_{\rm d}$ decreases, which is in accord with equation 17. Teyssandier et al. (2013) confirmed the action of this Kozai–Lidov mechanism at various parameters of the model.

4.2 3D simulations of planets on inclined orbits

We put a planet on inclined orbits with different inclination angles i_0 and two types of discs with $n = 1.5$ and 1.8 (see Table 5).

*4.2.1 Disc–planet interaction in model n*1.5*i*45

As an example, we take one of the reference models, $n1.5i45$, and show results for the disc–planet interaction in detail.

Top panels of Fig. 9 and the 3rd row from the top show that ELR waves form in the inner disc both in the surface density (top row) and the equatorial density distribution (3rd row). The $m = 2$ modes are clearly observed. The 2nd row shows the density distribution in the disc. The 4th row shows the equatorial density distribution, which decreases rapidly with radius. The bottom left-hand panels show that the eccentricity oscillates but increases on average up to $e \sim 0.7$–0.9 after $t \approx 70$. The inclination strongly oscillates and decreases on average. The bottom right-hand panels show the variation of the planet's coordinates (top) and the rz-slice of the density distribution (bottom). One can see that in equatorial x- and y-coordinates, the planet reaches the inner disc radius of $r \sim 1$–1.2, which leads to a variation of its eccentricity around a large value of $\sim$0.8. There are also large-scale variations of the x- and y-coordinates due to the precession of the orbit. The z-component decreases with time. The bottom right-hand panel shows that the disc is not symmetric about the equatorial plane due to the disc–planet interaction.

4.2.2 Models with n = 1.5 *and different* i_0

We took our reference model with $n = 1.5$ but placed a planet in orbits with different inclination angles: $i_0 = 5^\circ, 15^\circ, 30^\circ, 45^\circ, 60^\circ, 75^\circ$.

We observed that in models with relatively small inclination angles, $i_0 = 5^\circ$–30°, ELR resonances were excited in the inner disc, which are similar to those in the model with $i_0 = 0^\circ$. The eccentricity evolution and the growth rates are similar to those in the model with $i_0 = 0^\circ$ (see the top left-hand panel of Fig. 10). The bottom left-hand panel shows that the inclination angle decreased on average but strongly oscillates after time $t > 50$–70. At inclination angle $i_0 = 30^\circ$, the eccentricity increases faster than in models with smaller i_0.

At larger inclination angles, $i_0 = 45^\circ$ and 60°, the eccentricity initially strongly oscillates and reaches $e \approx 0.6$. Later, it increases to higher values of $e \approx 0.7$–0.9. The inclination of the orbit decreases on average and strongly oscillates (see right-hand panels in Fig. 10).

The top panels of Fig. 11 show variations in eccentricity and inclination, which were placed side by side on the same panels.

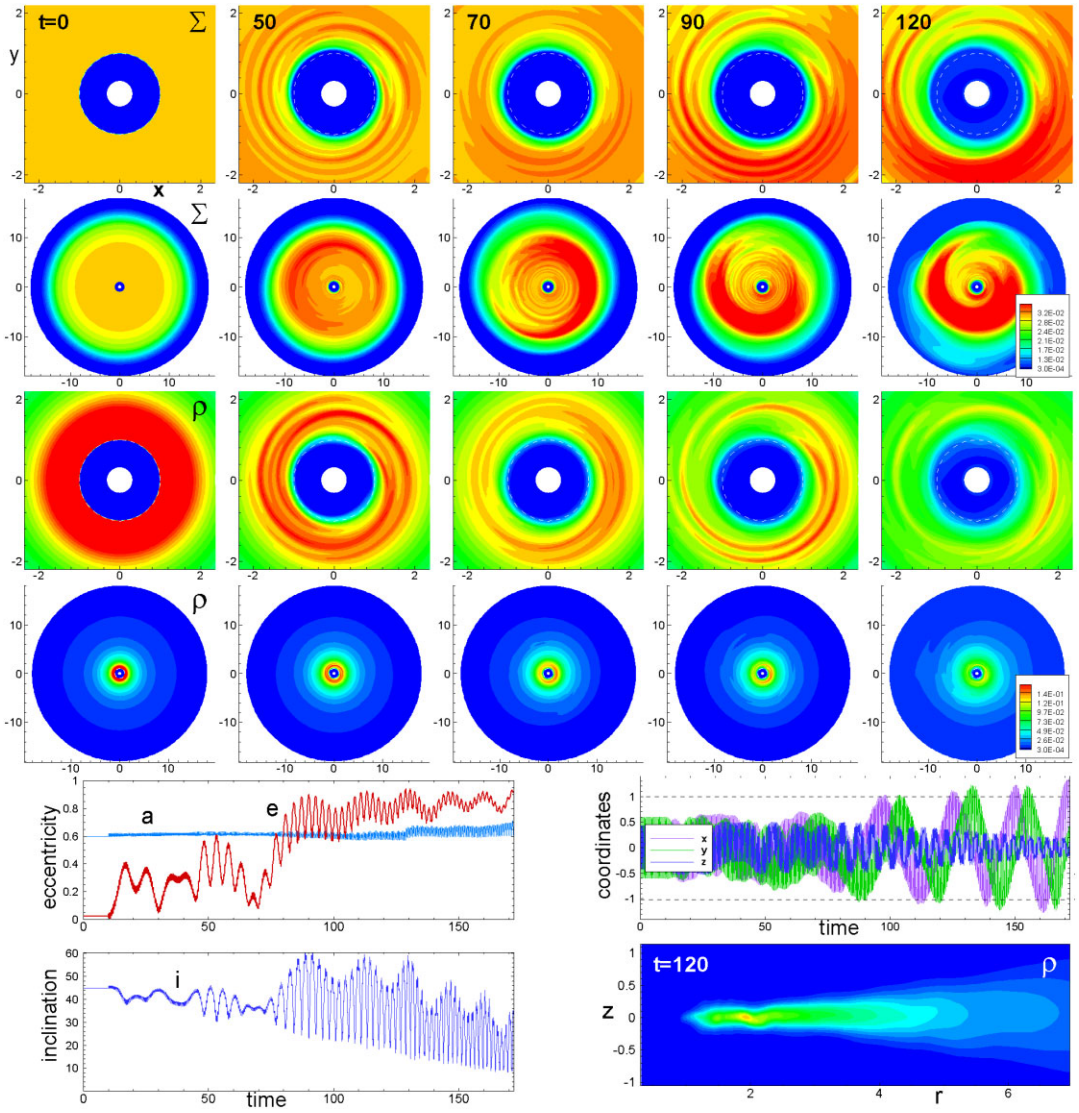

Figure 9. *T*op 4 rows: The same as in Fig. 2 but for the model $n1.5i45$. *Bottom left-hand panels*: Top: temporal evolution of the semimajor axis, a, and eccentricity, e. Bottom: temporal evolution of the inclination of the orbit, i. *Bottom right-hand panels:* Top: temporal evolution of the planet's coordinates, x, y, z. Bottom: density distribution in the rz-plane at $t = 120$.

The bottom panels show a part of the simulation time with a higher temporal resolution. One can see that the inclination and eccentricity oscillate in the antiphase, as predicted by the Kozai–Lidov mechanism. We observed such antiphase oscillations in all simulation runs with inclined orbits. We think we observe the eccentricity growth and its oscillations due to the Kozai–Lidov mechanism.

4.2.3 *Models with* $n = 1.8$ *and different* i_0

We repeat the above simulations using a reference model with a steeper density distribution, $n = 1.8$. The top left-hand panel of Fig. 12 shows that in models with relatively small inclination angles, $i_0 = 15^\circ$ and 30°, the eccentricity increases similar to that in the model with zero inclination ($n1.8i0$). However, the eccentricity increases $\sim$1.8 times slower compared with models where $n = 1.5$. The bottom left-hand panel shows that the inclination oscillates and decreases on average.

The right-hand panels of the same figure show the eccentricity and inclination in models with high inclination angles. One can see that the eccentricity strongly oscillates and reaches values of $e \approx 0.55$ in the model with $i_0 = 45^\circ$ and $e \approx 0.8$ in the model with $i_0 = 60^\circ$. The inclination angle also strongly oscillates and decreases on average. The time-scale of oscillations is $\sim$3 times longer in models with $n = 1.8$ compared with models $n = 1.5$. We suggest that this is because at $n = 1.8$, the disc has a lower mass compared with $n = 1.5$ models. Equation (17) from the theory shows that the time-scale of oscillations is inversely proportional to the mass of the disc, M_d. The mass of the disc in the model $n1.8i45$ is approximately 1.8 times smaller than that in the model $n1.5i45$. Comparisons show a correct tendency towards longer time-scales.

4.2.4 *Dependence of the maximum eccentricity* e_max *on* i_0

According to the theory, the maximum value of the eccentricity should increase with inclination of the orbit (see equation 15). From this equation, it follows that for inclinations $i_0 = 45^\circ, 60^\circ$, and 75°, the maximum eccentricities are $e_\mathrm{max} \approx 0.41, 0.76, 0.94$, respectively.

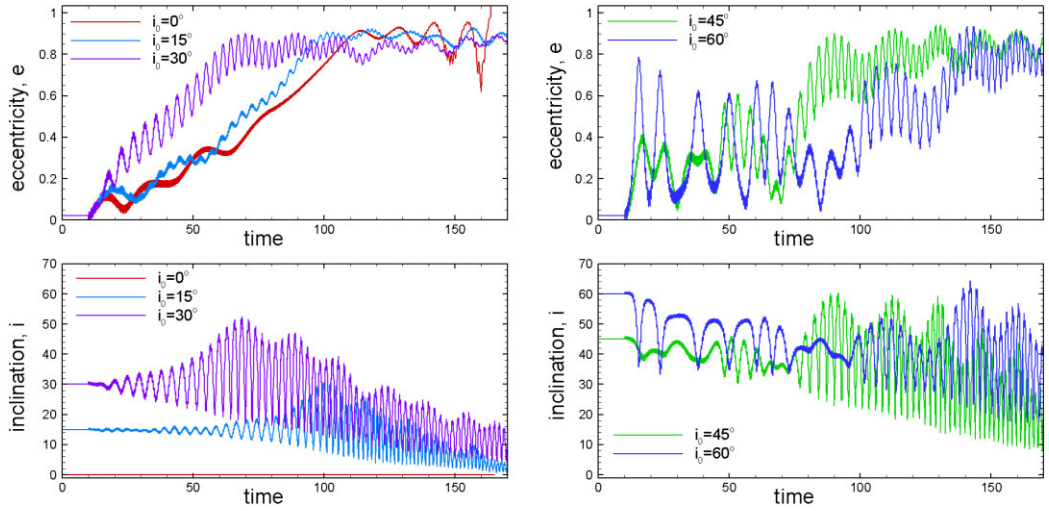

Figure 10. *Left-hand panels:* Temporal evolution of the eccentricity, e and inclination, i in models with $n = 1.5$ and initial values of the orbit inclination: $i_0 = 0°, 15°, 30°$. *Right-hand panels:* The same but for $i_0 = 45°, 60°$.

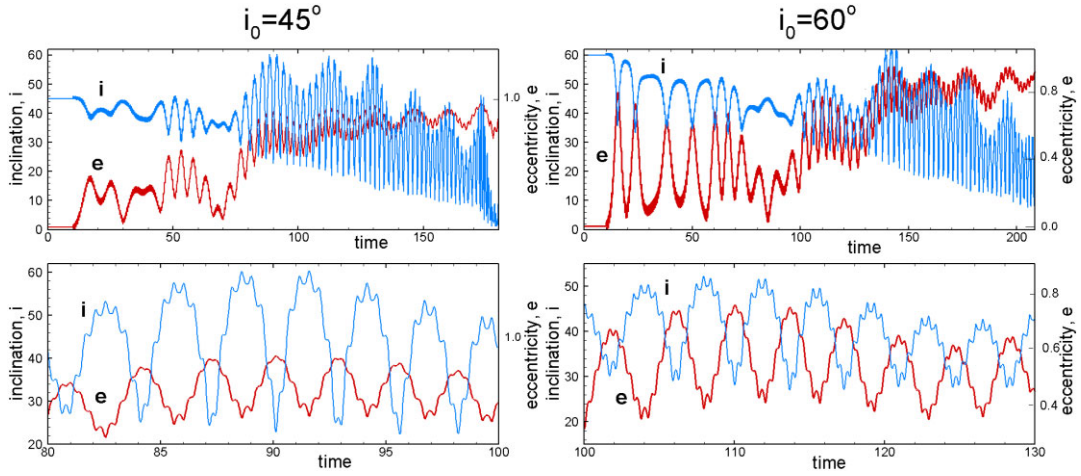

Figure 11. *Top panels:* Temporal evolution of the eccentricity, e and inclination, i in models *n1.5i45* and *n1.5i60*, where the eccentricity and inclination are shown at the same plot. *Bottom panels:* The same, but during shorter time intervals.

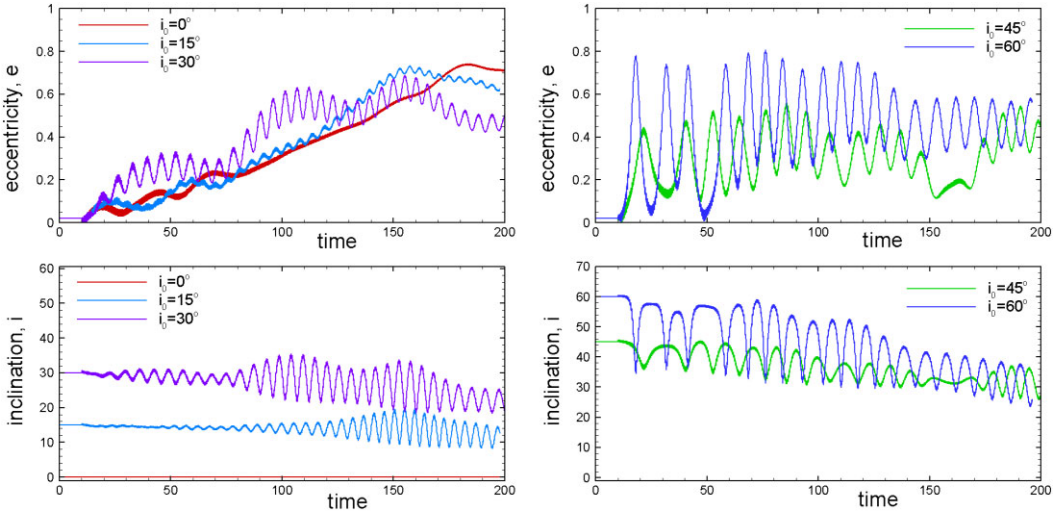

Figure 12. The same as in Fig. 10 but for reference models with $n = 1.8$ and different i_0.

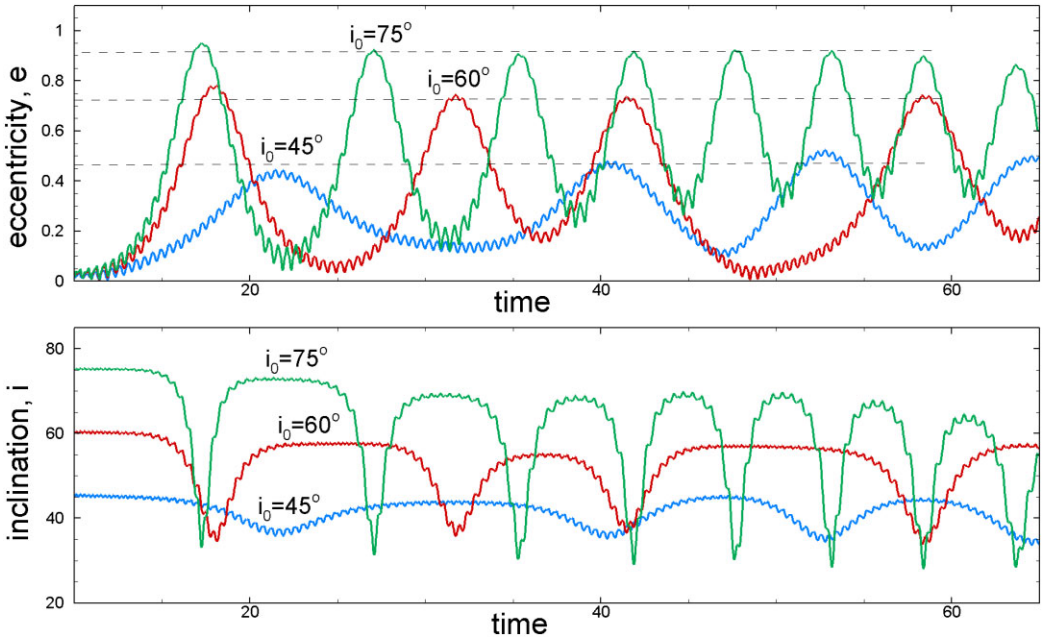

Figure 13. *Top panel:* Eccentricity evolution in the model with $n = 1.8$ at different initial values of the inclination angle of the orbit: $i_0 = 45°$, $60°$, and $75°$. Dashed horizontal lines show an approximate value of the eccentricity amplitude for each model. *Bottom panel:* Same, but for the inclination angle.

Table 6. Densities ρ_d and corresponding surface densities Σ_d used to derive the dependence of the oscillation time t_{osc} from the inner density of the disc (see Fig. 14).

Reference desity ρ_d	0.8	0.6	0.4	0.3	0.2	0.133	0.1	0.068	0.05
Reference surface density Σ_d	0.06	0.045	0.03	0.0225	0.015	0.01	0.0075	0.0051	0.00375

We took a model with $n = 1.8$ and compared maximum eccentricity values in models with $i_0 = 45°$, $60°$, and $75°$. We chose early moments before other processes started to influence the eccentricity growth. Top panel of Fig. 13 shows that e_{max} is larger in models with larger initial inclination. From the plot (see dashed horizontal lines in the plot), we obtain:: $e_{max} \approx 0.46, 0.73, 0.92$ for models with $i_0 = 45°$, $60°$, and $75°$, respectively. These values are very close to those predicted by the theory. We suggest that our model is close to the theoretical model by Terquem & Ajmia (2010) because at $n = 1.8$, most of the mass is in the outer regions of the disc, which is close to the theoretical model, where the disc is located far away from the planet. The bottom panel of Fig. 13 shows that the amplitude of inclination also increases with i_0.

4.2.5 *Time-scale of eccentricity growth in oscillations*

In this experiment, we fix the disc radii and structure but change the reference surface density Σ_d (see Table 6). This way, we change the mass of the disc. We observed that the time-scale of oscillations increases when Σ_d decreases. Fig. 14 shows the dependence of the period of oscillations t_{osc} on $1/\Sigma_d$ is similar in models with $n = 1.5$ and 1.8. The dependence is approximately linear for $1/\Sigma_d \gtrsim 100$. From the plot, we derive an approximate dependence:

$$t_{osc} \approx 0.53\left(\Sigma_d^{-1} - 18\right). \quad (19)$$

At small values of Σ_d, we obtain $t_{osc} \approx 0.53\Sigma_d^{-1}$. In our models, the mass of the disc $M_d \sim \Sigma_d$ and therefore, $t_{osc} \sim 1/M_d$, as predicted in theoretical models (see equation 17).

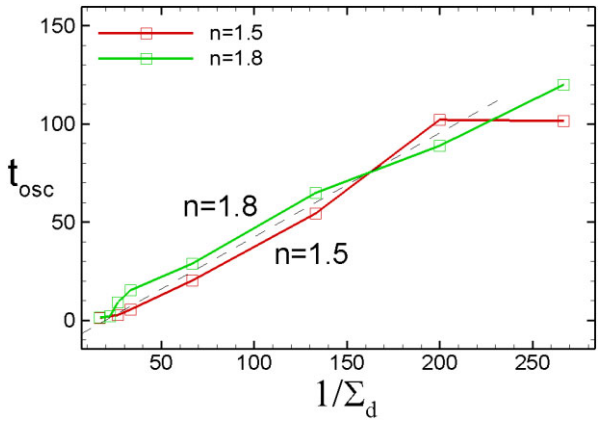

Figure 14. Period of Kozai–Lidov oscillations obtained in simulations of discs with different initial surface densities in models $n1.5i45$ and $n1.8i45$. The dashed line shows the dependence taken for analytical estimates and projections in equations (17) and (20).

Equation (19) is in dimensionless units. For practical applications, we convert this equation to dimensional units using the projected value of the characteristic disc mass of $\Sigma_d = 10^{-4}$. We take into account that we measure time in rotational periods at $r = r_{cav}$ and take $r_{cav} = 10$ au as a reference scale (see Table 1), and obtain:

$$T_{osc} \approx 3.18 \times 10^5 \mathrm{yr}\left(\frac{r_{cav}}{10\,\mathrm{au}}\right)^{3/2}\left(\frac{\Sigma_d}{10^{-4}}\right)^{-1}. \quad (20)$$

This time-scale is comparable with the time-scale of eccentricity growth due to ELRs (see equation 12).

Table 7. The mode number m, type of resonance, res, resonant radii $r_{\rm res}/a_{\rm p}$, coefficients $\mathcal{A}$ and $\mathcal{B}$ for ELRs and their ratios.

m	res	$r_{\rm res}/a_{\rm p}$	$\mathcal{A}$	$\mathcal{B}$	$\mathcal{A}/\mathcal{B}$
2	1:3	2.080	0.607	1.849	0.328
3	2:4	1.587	5.201	3.594	1.447
4	3:5	1.406	7.362	5.604	1.314

We also compared the time-scale of eccentricity growth $t_{\rm ev}$ given by the theory (see equations 16–18) with that obtained in our simulations. As an example, we use a model $n1.5i60$, which shows high-amplitude oscillations, and consider the 3rd peak in the eccentricity curve shown in the top right-hand panel of Fig. 11 (we take one of the early moments when the disc is approximately homogeneous and the density wave did not form yet). In the 3-rd peak $e_0 \approx 0.1$, $e_{\rm max} \approx 0.6$. We take $a_{\rm p} = 0.6$ and $R_{\rm d} = 13$ (the radius of exponential cut) and obtain $\eta \approx 0.077$. We also obtain $K \approx 0.041$, $t_{\rm ev}/\tau \approx 1.27$. We calculate the dimensionless mass of the disc as $M_{\rm d} \approx 15.8$ and obtain the final value of time in our dimensionless units as $t_{\rm ev} \approx 15.7$. We compare this value with the time of eccentricity growth in the 3rd peak obtained from the figure, which is $t_{\rm sim} \approx 9$. One can see that the difference is in the factor of 1.7, which is in reasonable agreement with the theory.

5 ECCENTRICITY OF THE DISC AND PRECESSION

A planet on the eccentric orbit excites eccentricity in the disc (e.g. Ogilvie 2007). The linear analysis (performed for small eccentricities of the planet and the disc) shows that the eccentricities of the planet and the disc are coupled through resonant interactions (e.g. Ogilvie 2007; Teyssandier & Ogilvie 2016). To compare our results with theory, we use formulae for the temporal evolution of complex eccentricities from Teyssandier & Ogilvie (2016) (see their equations 14 and 15). A single ELR contributes to the evolution of eccentricities of the planet and the disc (in the vicinity of the resonance) in the following way:

$$M_{\rm p} a_{\rm p}^2 \Omega_{\rm p} \left(\frac{\partial E_{\rm p}}{\partial t}\right)_{\rm ELR} = \frac{G M_{\rm p}^2}{M_\star} E_{\rm p} \mathcal{B}^2 \left(1 - \frac{\mathcal{A} E_{\rm d}}{\mathcal{B} E_{\rm d}}\right) \int \Sigma F 2\pi r \, {\rm d}r, \tag{21}$$

$$\Sigma r^2 \Omega \left(\frac{\partial E_{\rm d}}{\partial t}\right)_{\rm ELR} = -\frac{G M_{\rm p}^2}{M_\star} \Sigma \mathcal{A}\mathcal{B} E_{\rm p} \left(1 - \frac{\mathcal{A} E_{\rm d}}{\mathcal{B} E_{\rm p}}\right) F, \tag{22}$$

where $E_{\rm p} = e_{\rm p} {\rm e}^{i\bar{w}_{\rm p}}$ and $E_{\rm d} = e_{\rm d} {\rm e}^{i\bar{w}_{\rm d}}$, $e_{\rm p} = |E_{\rm p}|$, $e_{\rm d} = |E_{\rm d}|$; $\bar{w}_{\rm p}$ and $\bar{w}_{\rm d}$ are the arguments of the pericentre of the planet's and disc's semimajor axes, respectively. Here, $F = w_{\rm L}^{-1} \Delta[(r - r_{\rm res})/w_{\rm L} - 1]$ is a function of resonant radius $r_{\rm res}$, resonant width $w_{\rm L}$ and dimensionless function Δ. Values $w_{\rm L}$ and function Δ describe the radial profile of the ELR resonance.

In our simulations, we observe formation of ELR waves with mode numbers $m = 2, 3$ and sometimes $m = 4$. Table 7 shows the values of coefficients $\mathcal{A}$ and $\mathcal{B}$ for these resonaces and the resonant radii $r_{\rm res}$ (see an extended version of the table in Teyssandier & Ogilvie 2016).

In the above sections, we calculated the evolution of the planet's eccentricity. Below, we study the disc eccentricity and precession of the planet and disc.

5.1 Disc eccentricity

We calculate the distribution of the disc eccentricity with radius using an approach based on the angular momentum deficit (hereafter AMD) $A_{\rm d}(r)$ (e.g. Ragusa et al. 2018). The angular momentum deficit of the ring is $A_{\rm d}(r) = J_{\rm circ}(r) - J_{\rm d}(r)$, where

$$J_{\rm circ}(r) = \int \Sigma \sqrt{GMa} \, {\rm d}\phi, \quad a = -\frac{GM}{2E}, \quad E = -\frac{GM}{r} + \frac{v^2}{2}$$

is the circular angular momentum of the ring in the disc located at radius r, and $J_{\rm d}(r) = \int \Sigma r v_\phi \, {\rm d}\phi$. is the real angular momentum of the ring at the radius r. The eccentricity of the ring is

$$e_{\rm d}(r) = \sqrt{\frac{2A_{\rm d}(r)}{J_{\rm circ}(r)}}. \tag{23}$$

Our disc has a finite thickness and therefore is not precisely Keplerian due to the pressure component. In the calculation of the disc eccentricity, we subtracted this background eccentricity (see also Ragusa et al. 2024).

Fig. 15 shows the distribution of $e_{\rm d}(r)$ at different moments in time in models $n1.5i0$ and $n1.8i0$ (see left-hand and right-hand panels, respectively). In both models, the disc eccentricity is larger in the inner disc (in the region of ELRs). Eccentricity in the inner disc increases with time in both models. Eccentricity in the rest of the disc increases most of the time in the model $n1.5i0$ and reaches $e_{\rm d} \approx 0.1$ on average at $t = 110$. In the model $n1.8i0$, the disc eccentricity varies and is $e_{\rm d} \approx 0.05$–0.06 on average.

Next, we calculate the evolution of eccentricity with time. For that, we take the average eccentricity value in some radii interval. The left-hand panel of Fig. 16 shows the temporal evolution of eccentricity where we took the averaged value in the interval of radii $1 < r < 3$ (where ELR resonances are located). One can see that the inner disc eccentricity gradually increases in both models. The right-hand panel shows the temporal variation of eccentricities averaged at $1 < r < 12$. One can see that the eccentricity of the whole disc varies quasi-periodically, with a quasi-period of 30–40 in model $n1.5i0$ and a slightly longer quasi-period in model $n1.8i0$.

Now, we can compare simulation results with theoretical expectations. Here, we neglect the precession and take the absolute values, $e_{\rm p} = |E_{\rm p}|$ and $e_{\rm d} = |E_{\rm d}|$ (like we did in R23). According to the theory (see equation 21), the planet's eccentricity will increase if the value in the brackets $(1 - \mathcal{A} e_{\rm d}/\mathcal{B} e_{\rm p}) > 0$, that is if $e_{\rm p} > \mathcal{A}/\mathcal{B} e_{\rm d}$. As an example, we take a model $n1.5i0$ and some moment in time $t = 50$. From the left bottom panel of Fig. 2, we obtain the planet eccentricity $e_{\rm p} \approx 0.25$, and from the left-hand panel of Fig. 16, the inner disc eccentricity: $e_{\rm d} \approx 0.025$. Simulations show that at this time, ELR 1:3 resonance dominates ($m = 2$). Taking the value of $\mathcal{A}/\mathcal{B}$ for 1:3 resonance from Table 7 and $e_{\rm d} = 0.025$, we obtain that condition for planet eccentricity growth becomes $e_{\rm p} > 0.008$. This condition is satisfied, and the planet's eccentricity will grow. Comparisons at other times show a similar result, and therefore in our model, conditions are always favourable for the planet's eccentricity growth.

Similar estimates for the disc eccentricity growth (see equation 22) show that the disc eccentricity cannot grow at any values of $e_{\rm d}$ and $e_{\rm p}$ obtained in simulations. We suggest that relatively small eccentricities of the disc observed in our simulations may be connected with this theoretical prediction.

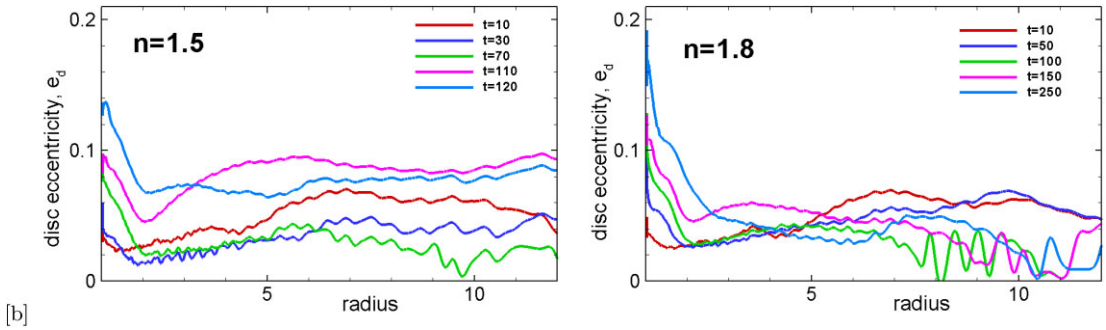

Figure 15. Radial distribution of the disc eccentricity at different moments of time obtained in models $n1.5i0$ (left-hand panel) and $n1.8i0$ (right-hand panel).

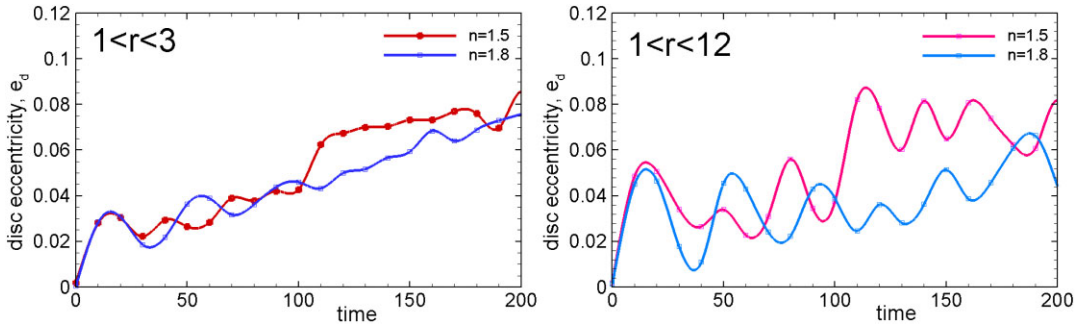

Figure 16. *Left-hand panel:* Temporal variation of the averaged eccentricity of the disc $\bar{e_{\rm d}}$ in models $n1.5i0$ and $n1.8i0$ calculated for the inner part of the disc in the interval of radii $1 < r < 3$. *Right-hand panel:* Same, but for the disc eccentricity taken in the interval of radii $1 < r < 12$.

5.2 Precession

Simulations show that the planet's orbit precesses counterclockwise. The bottom left-hand panels of Figs 2 and 3 show coordinates x and y of the planet's orbit in the equatorial plane. The waves in the curve reflect the precession of the planet. The amplitude of waves increases due to the increase of eccentricity. Period of planet precession is $T_{\rm prec} \approx 25$–30 in model $n1.5i0$ and $T_{\rm prec} \approx 30$–35 in model $n1.8i0$. Test simulations of model $n1.5i0$ at a twice as low and high inner surface density of the disc $\Sigma_{\rm d} = 0.015$ and 0.06 have shown that the period of precession is larger in models with a lower density of the disc. The disc also precesses. The precession can be tracked using the orientation of the density wave seen in the surface density distributions (see Fig. 2).[5]

Fig. 17 shows an episode of precession in models $n1.5i0$ and $n1.8i0$ in greater detail. The top left-hand panels show the time sequence of the surface density distribution during an interval of time $\Delta t = 80$–110 in model $n1.5i0$. It shows that the density wave in the disc precesses counterclockwise with a period of $T_{\rm prec} \approx 25$–30. The bottom left-hand panel shows that a planet precesses approximately with the same period.

Right top panels of Fig. 17 show the same but for the model $n1.8i0$. The top panels show that the spiral wave is only slightly visible. We suggest that in this model, where the surface density decreases with radius, lines of pericentres become aligned more rapidly than in the previous model of homogeneous disc. The bottom panel shows that the planet precesses with a period of $T_{\rm prec} \approx 30$–35.

According to equations (21) and (22), the precession of the planet and disc can influence the rate of eccentricity growth (Teyssandier & Ogilvie 2016). From simulations, we see that the planet and disc precess couterclockwise approximately at the same rate. If they precess with precisely the same rate and have the same phase, then $\bar{w}_{\rm p} - \bar{w}_{\rm d} = 0$ and $e^{i(\bar{w}_{\rm p} - \bar{w}_{\rm d})} = 1$. In the opposite situation, if they precess in antiphase, $\omega_{\rm p} - \omega_{\rm d} = \pi$ and $e^{i(\omega_{\rm d} - \omega_{\rm p})} = -1$. In both cases, the value in brackets in the right-hand side of equation (21) is positive and planet's eccentricity will grow.

6 CONCLUSIONS

We have investigated the evolution of the eccentricity of massive planets located inside cavities of protoplanetary discs. The main conclusions are the following:

(1) **In models with aligned orbits** ($i_0 = 0$):

(a) The eccentricity increases up to high values of $e \sim 0.7$–0.9 due to the ELR resonances excited in the inner disc. Resonances with modes $m = 2$ and 3 dominate. The eccentricity increases any time when ELR waves are excited in the disc. This process is similar to that observed in 2D simulations of R23.

(b) The characteristic time of eccentricity growth increases in models with smaller planet mass due to smaller torque acting on the disc. The amplitude of ELR waves is smaller in models with smaller planet mass.

(c) At higher viscosity in the disc, the ELR density waves become smeared, and eccentricity growth decreases.

[5]The density wave tracks the precession of the disc only approximately. Teyssandier & Ogilvie (2016) note that eccentricity excited in the inner parts of the disc propagates out in the form of a one-armed density wave. It is probable that the density wave results from the fact that initially, the rings of matter in the disc have different precession rates and different lines of percenters, which are more aligned in the inner parts of the disc where processes are faster (see an illustration of this effect in fig. 1 of Ragusa et al. 2024).

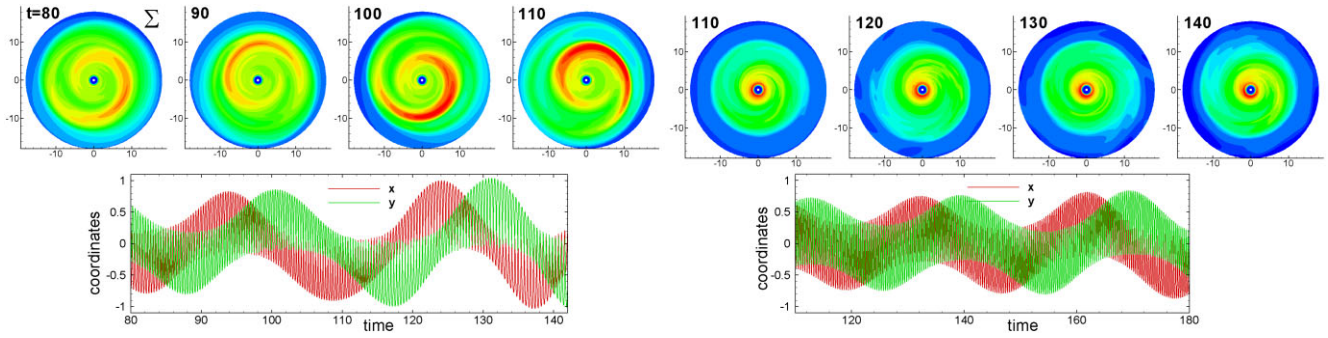

Figure 17. *Top panels:* Density distribution in the disc during the sequence of times shows the precession of the disc in models $n1.5i0$ (left four panels) and $n1.8i0$ (right four panels). *Bottom panels:* Variation of xy-coordinates of the planet in the equatorial plane shows the precession of the planet.

(d) The grid resolution is an essential factor. At a low grid resolution, the number of grids could not be sufficient to resolve ELR waves. In addition, the amplitude of density waves decreases due to the numerical diffusivity.

(e) The disc eccentricity slowly increases with time, with the largest eccentricity at the inner disc. It increases with the growth of the planet's eccentricity. Planet–disc interaction leads to the precession of the planet's orbit. The density waves or other inhomogeneities in the disc precess with comparable period. Disc eccentricity and its influence on the planet's orbit should be further studied in models with lower disc density and longer simulation runs.

(2) **In models with inclined orbits** ($i_0 \neq 0$):

(a) At relatively small inclination angles, $i_0 \lesssim 30^\circ$, the eccentricity increases up to $e \sim 0.7$–0.9 due to the ELRs, like in models with $i_0 = 0$. The Kozai–Lidov oscillations of small amplitude are observed. The orbital inclination decreases on average.

(b) At large inclination angles, $i_0 = 45^\circ$, 60°, and 90° eccentricity and inclination strongly oscillate in the antiphase, like in the original Kozai–Lidov mechanism.

(c) The amplitude of oscillations increases when i_0 increases and reaches $e \approx 0.9$ in the case of $i_0 = 75^\circ$. The time-scale of eccentricity growth increases when the characteristic disc's mass decreases.

(d) Eccentricity may also increase on average due to ELRs.

The above simulations show good potential for explaining the eccentricity of exoplanets, including very high eccentricities. However, the final eccentricity at the time of disc dispersal can be different, and it depends on a number of factors. One of the important factors is the size of the disc-cavity boundary. At relatively small sizes, say, at $r_{\rm cav} \lesssim 10$ au, the eccentricity increases rapidly, and the planet may enter the inner disc and lose eccentricity due to the local corotation torque. Later, if the disc moves away, the eccentricity may increase again. Therefore, several episodes of eccentricity growth and decay may occur. In the case of planets on inclined orbits, several Kozai–Lidov cycles of eccentricity oscillation are expected. On the other hand, for cavities located at much larger distances, the eccentricity increases slowly, and only a part of the eccentricity growth cycle is expected.

Our simulations were performed at a high density (and mass) of the disc, which provided higher torques between the planet and the disc and helped to decrease computing time. We scale simulations to lower densities and longer time-scales using the theoretical prediction that the eccentricity growth rate is inversely proportional to the density (e.g. Goldreich & Tremaine 1980) and results of 2D simulations of R23, which confirmed this dependence. Future 3D simulations should be done at the lower density in the disc and also in discs with a steeper density distribution.

ACKNOWLEDGEMENTS

The authors thank the anonymous referee for valuable recommendations. Resources supporting this work were provided by the NASA High-End Computing (HEC) Program through the NASA Advanced Supercomputing (NAS) Division at Ames Research Center and the NASA Center for Computational Sciences (NCCS) at Goddard Space Flight Center. MMR and RVEL were supported in part by the NSF grant AST-2009820. C. Espaillat was supported in part by NASA ADAP 80NSSC20K0451.

DATA AVAILABILITY

The data underlying this article will be shared on reasonable request to the corresponding author (MMR).

REFERENCES

Anderson K. R., Lai D., 2017, MNRAS, 472, 3692
Anderson K. R., Storch N. I., Lai D., 2016, MNRAS, 456, 3671
Anderson K. R., Lai D., Pu B., 2020, MNRAS, 491, 1369
Artymowicz P., Clarke C. J., Lubow S. H., Pringle J. E., 1991, ApJ, 370, L35
Bai X.-N., 2016, ApJ, 821, 80
Baruteau C., Wafflard-Fernandez G., Le Gal R., Debras F., Carmona A., Fuente A., Riviere-Marichalar P., 2021, MNRAS, 505, 359
Bitsch B., Crida A., Libert A.-S., Lega E., 2013a, A&A, 555, A124
Bitsch B., Crida A., Morbidelli A., Kley W., Dobbs-Dixon I., 2013b, A&A, 549, A124
Chatterjee S., Ford E. B., Matsumura S., Rasio F. A., 2008, ApJ, 686, 580
Comins M. L., Romanova M. M., Koldoba A. V., Ustyugova G. V., Blinova A. A., Lovelace R. V. E., 2016, MNRAS, 459, 3482
Debras F., Baruteau C., Donati J.-F., 2021, MNRAS, 500, 1621
Dullemond C. P., Hollenbach D., Kamp I., D'Alessio P., 2007, Protostars and Planets V. Univ. Arizona Press, Tucson
Dunhill A. C., Alexander R. D., Armitage P. J., 2013, MNRAS, 428, 3072
DÁngelo G., Lubow S. H., Bate M. R., 2006, ApJ, 652, 1698
Elbakyan V., Wu Y., Nayakshin S., Rosotti G., 2022, MNRAS, 515, 3113
Fabrycky D., Tremaine S., 2007, ApJ, 669, 1298
Fromang S., Terquem C., Nelson R. P., 2005, MNRAS, 363, 943
Goldreich P., Sari R., 2003, ApJ, 585, 1024
Goldreich P., Tremaine S., 1979, ApJ, 233, 857
Goldreich P., Tremaine S., 1980, ApJ, 241, 425

Hartmann L., 2000, Accretion Processes in Star Formation, Vol. 32. Cambridge Univ. Press, Cambridge
Holman M., Touma J., Tremaine S., 1997, Nature, 386, 254
Innanen K. A., Zheng J. Q., Mikkola S., Valtonen M. J., 1997, AJ, 113, 1915
Jurić M., Tremaine S., 2008, ApJ, 686, 603
Kane S. R., Ciardi D. R., Gelino D. M., von Braun K., 2012, MNRAS, 425, 757
Kley W., 1998, A&A, 338, L37
Kley W., Dirksen G., 2006, A&A, 447, 369
Kley W., Nelson R. P., 2012, ARA&A, 50, 211
Koldoba A. V., Ustyugova G. V., Lii P. S., Comins M. L., Dyda S., Romanova M. M., Lovelace R. V. E., 2016, New Astron., 45, 60
Königl A., 1991, ApJ, 370, L39
Kozai Y., 1962, AJ, 67, 591
Li J., Lai D., 2023, ApJ, 956, 17
Li J., Lai D., Anderson K. R., Pu B., 2021, MNRAS, 501, 1621
Lidov M. L., 1962, Planet. Space Sci., 9, 719
Lin D. N. C., Ida S., 1997, ApJ, 477, 781
Lovelace R. V. E., Romanova M. M., Barnard A. W., 2008, MNRAS, 389, 1233
Marcy G., Butler R. P., Fischer D., Vogt S., Wright J. T., Tinney C. G., Jones H. R. A., 2005, Prog. Theor. Phys. Suppl., 158, 24
Masset F. S., 2000, A&AS, 141, 165
Masset F. S., Morbidelli A., Crida A., Ferreira J., 2006, ApJ, 642, 478
Mustill A. J., Davies M. B., Johansen A., 2017, MNRAS, 468, 3000
Ogilvie G. I., 2007, MNRAS, 374, 131
Ogilvie G. I., Lubow S. H., 2003, ApJ, 587, 398
Papaloizou J. C. B., Terquem C., 2001, MNRAS, 325, 221
Papaloizou J. C. B., Nelson R. P., Masset F., 2001, A&A, 366, 236
Pierens A., Raymond S. N., 2016, MNRAS, 462, 4130
Ragusa E., Rosotti G., Teyssandier J., Booth R., Clarke C.J., Lodato G., 2018, MNRAS, 474, 4460
Ragusa E., Lynch E., Laibe G., Longarini C., Ceppi S., 2024, A&A, 686, A264
Rasio F. A., Ford E. B., 1996, Science, 274, 954
Rice W. K. M., Armitage P. J., Hogg D. F., 2008, MNRAS, 384, 1242
Romanova M. M., Lovelace R. V. E., 2006, ApJ, 645, L73
Romanova M. M., Owocki S. P., 2015, Space Sci. Rev., 191, 339
Romanova M. M., Lii P. S., Koldoba A. V., Ustyugova G. V., Blinova A. A., Lovelace R. V. E., Kaltenegger L., 2018, MNRAS, 485, 2666
Romanova M. M., Koldoba A. V., Ustyugova G. V., Lai D., Lovelace R. V. E., 2023, MNRAS, 523, 2832 (R23)
Sagear S., Ballard S., 2023, PNAS, 120, e2217398120
Schnepf N. R., Lovelace R. V. E., Romanova M. M., Airapetian V. S., 2015, MNRAS, 448, 1628
Shakura N. I., Sunyaev R. A., 1973, A&A, 24, 337
Takeda G., Rasio F. A., 2005, ApJ, 627, 1001
Terquem C., Ajmia A., 2010, MNRAS, 404, 409
Teyssandier J., Ogilvie G. I., 2016, MNRAS, 458, 3221
Teyssandier J., Terquem C., Papaloizou C. B., 2013, MNRAS, 428, 658
Wang L., Goodman J. J., 2017, ApJ, 835, 59

This paper has been typeset from a TEX/LATEX file prepared by the author.